Investigations on the fracture behavior of Inconel 718 superalloys obtained from cast and additive manufacturing processes

Benoît Vieille, Clément Keller, M. Mokhtari, H. Briatta, T. Breteau, Josiane Nguejio, Mouldi Ben Azzouna, Fabrice Barbe, E. Baustert

Investigations on the fracture behavior of Inconel 718 superalloys obtained from cast and additive manufacturing processes

B. Vieille[1], C. Keller[1], M. Mokhtari[1], H. Briatta[1], T. Breteau[1,2], J. Nguejio[1], F. Barbe[1], M. Ben Azzouna[1], E. Baustert[2]

1 GPM, INSA Rouen Normandie, UMR CNRS 6634, Université de Rouen, 76800 St Etienne du Rouvray

2 Volum-E, 1 Chemin de la Fonderie, 76340 Blangy-sur-Bresle

Address correspondence to : benoit.vieille@insa-rouen.fr

Abstract

This paper examines the effects of manufacturing processes on the fracture behavior of Inconel 718 alloy at room temperature. This comparative study was conducted on specimens obtained from cast and PBF (Power Bed Fusion) additive manufacturing. Mechanical testing was conducted on single edge notch specimens in bending. In order to quantify the influence of the manufacturing process on the fracture behavior, the *J-R* curves were obtained from the energy per unit of fracture surface area needed to drive crack growth in agreement with the ASTM standard E1820-01. Depending on the specimen type and the location of the initial notch with respect to the lasing planes, crack initiation significantly differs resulting from specific microstructures. These differences may explain why AM specimens have much higher fracture toughness at initiation (about 70 to 100%) and subsequent crack propagation. The *in situ* crack propagation was studied via the observations of the crack path along with the mechanical loading. An original picture analysis was developed to monitor the crack growth based on the location of the crack tip at specimen surface.

Keywords: fracture toughness, ductility, cast, Additive Manufacturing, microstructure

1. Introduction

Inconel 718 alloys are high-strength nickel-base superalloys which are widely used as structural components under high-temperature and relatively high stress conditions. A potential premature failure exists if crack-like defects of sufficient size and shape are present at critical locations [1]. The fracture behaviors of conventional cast and forged Inconel 718 alloys have been extensively studied since the seventies [2-6]. Due to their complex metallurgical microstructure, involving precipitation of several phases, their fracture behavior is strongly influenced by heat treatment [1], alloy composition and manufacturing processes [3]. Depending on the microstructure (hence the heat treatments), significant differences in the J-R curves were observed. Fracture toughness tests are conventionally performed using linear-elastic (K_{Ic}) and elastic-plastic (J_{Ic}) fracture mechanic approaches. Most of the references available in the literature have specifically discussed the relationship between key microstructural features, fracture mechanisms and macroscopic properties based on metallographic and fractographic analyses [2][7-9].

With the emergence of additive manufacturing parts in cutting-edge applications, it is necessary to better understand the Inconel 718 fracture behavior and properties. These are expected to significantly differ from the cast materials. Additive manufacturing (AM) by PBF is of great interest given its ability to produce complex and non-conventional geometries; however, microstructures generated by this process can differ significantly from their conventionally developed counterparts (e.g. cast and forged materials). Depending on the manufacturing parameters (e.g. laser velocity and power), this process is based on a spatially and temporally mobile heat source. This heat source may cause the development of significant microstructural heterogeneity: a mixture of columnar (elongated) and equiaxed (isotropic) grains, often with a visible periodicity corresponding to the layer height, the hatch distance and scanning pattern used [10-11]. To these microstructural heterogeneities are associated crystallographic textures that influence the mechanical behaviour of the parts [12-13]. The

choice of trajectories, and also specific manufacturing parameters (thickness of the powder to be fused, the power and speed of the laser) define the construction strategy of a part. The control of the heat source is therefore essential to control the solidified grain structure, and obtain optimal microstructures for the targeted applications.

1.1 Microstructure and mechanical behavior

The AM-PBF process involves high solidification rates and high temperature gradients. Cooling rates are therefore also very important, causing the formation of microstructures that can deviate significantly from the thermodynamic equilibrium. In the case of nickel-based superalloy industrial alloys (e.g. Inconel 718), this may cause undesirable sequences. Indeed, the precipitation of intermetallic phases from the liquid state, to hardened solid solutions of composition very far from the thermodynamic equilibrium, without or with few precipitated phases, are observed. Unexpected primary solidification structures or morphologies significantly different from those produced by more conventional processes may also appear [10][14-17]. Most of the studies available in the literature underline the importance of heat treatments on both microstructure and mechanical properties of Inconel 718. These references illustrate the capability of the PBF-process to produce parts with mechanical properties better than forged and cast material at room temperature and equal properties to forged material at elevated temperatures with a high proportion of intragranular δ Laves phases in the PBF-processed material [18]. More specifically, the fatigue cracks stopped in front or detoured around the Laves phases. This means that the unbroken Laves phases play an important role in hindering crack propagation [19].

Most references on Inconel 718 obtained from PBF address the relationship between its microstructure and the common mechanical properties (hardness, tensile properties) [20-28] and fatigue crack growth [19][29-37]. From the comparison with cast and forged Inconel 718, these references indicate a trend regarding the changes in the mechanical properties in

tension. Due to the presence of interdentritic precipitates and the development of γ' and γ'' phases, the as-fabricated AM samples are characterized by finer dislocated cellular structures, higher ductility and transgranular ductile fractures in tension [16][28]. After standard solution and ageing treatments of PBF manufactured 718 superalloys, a transgranular ductile fracture is also observed. Their tensile properties are about the same with respect to cast and forged Inconel 718; however, their ductility dramatically decreased resulting from the precipitation of fine γ' and γ'' phases in the austenitic matrix and needle-like δ phases inside the grain and at the grain boundaries [19][28].

1.2 Microstructure and fracture behaviour

Very few studies have specifically addressed the fracture toughness of metallic materials produced by AM [38-40]. As reviewed in literature [13], orientation-dependent microstructures, texture, and defects result in different tensile properties and even more significant differences in the fracture-critical properties (e.g. fatigue crack growth, fracture toughness). Indeed, the PBF process may induce microstructures with columnar architectures, parallel to the building z-direction (along the heat flow direction). In the x-y plane, a unique structural morphology was observed using different cooling rates resulting from laser beam overlapping. Post-processing (e.g., heat treatment and/or Hot Isostatic Pressing) can reduce or eliminate process-induced defects (e.g. lack of fusion and porosities) but conversely influence the additive manufactured materials cost [41]. These post-processing treatments also contribute to the reorganization of the highly textured columnar structure into fine columnar and/or equiaxed grains (whose average grain size is about a hundred μm) of random orientations. Based on Single-Edge- Notch Bending (SENB) tests conducted by means of a Charpy impact pendulum, the fracture toughness of AM specimens appear to be close to that reported in Inconel weld metal ones [39].

1.3 Objectives of the study

This study is expected to be helpful to engineers willing to design Inconel 718 parts, processed by Additive Manufacturing, for structural applications. Considering the lack of knowledge on the fracture behavior and toughness of additive manufactured nickel-base superalloys 718, this study proposes an original contribution to the comparison of cast and PBF materials via: (i) an evaluation of the mode I fracture toughness at room temperature – (ii) an accurate *in situ* monitoring of the crack propagation based on digital picture analyses – (iii) an insight into the fracture mechanisms associated with fractographic examinations. Ultimately, the purpose is to better understand how the microstructure induced by additive manufacturing is related to the ductile fracture behavior of Inconel 718. In order to focus on the fracture properties and behavior of cast and AM materials, all specimens were tested as received, with no prior heat treatment.

The paper is organized as follows. After a brief introduction of the studied materials, the experimental procedure will be detailed. A particular attention will be paid to the presentation of the digital image analysis from which the *in situ* crack growth was evaluated during mechanical loading. Then, the J-R curves were obtained from the image analysis and the computation of the fracture toughness from the ASTM E1820-01 standard test method [42]. Finally, these curves are discussed along with the fractographic examination of fracture surfaces.

2. Materials and experimental procedure

2.1 Materials

Cast and additive manufactured Inconel 718 alloys are studied. The chemical compositions of this alloy are given by the providers in Tables 1 and 2 for cast and AM materials, respectively. The cast round bars of IN718 are made by means of Vacuum Induction Melting (VIM) followed by Vacuum Arc Remelting (VAR) in order to produce the desired alloy composition.

The VIM process insures the entire bulk of the alloy to be liquid. The VIM process can accomplish a degree of refining by removing oxides and nitrides.

Their tensile mechanical properties are presented in Table 3. Cast round bars and AM specimens were tested as received (with no heat treatment). It is therefore expected that the mechanical behavior and properties significantly differ between cast and AM specimens. AM Inconel 718 blocks (35x100x100mm^3) were manufactured by Company VolumE with an EOS M400-4 PBF machine under argon from a powder whose particles average diameter is about 30µm. The laser scanning speed and power, as well as the hatch distance used for blocks manufacturing are indicated in Table 4. The porosity rate of AM specimens is about 0.27%. It was calculated from the specimen density measured by means of a Sartorius Secura densimeter whose accuracy is about 1 mg. Both types of materials were machined into parallelepipedic samples (Fig. 1) in agreement with the ASTM E1820-01 standard test method [42]. The edge notch was machined by means of a precision endless diamond wire saw whose radius is 0.085 mm.

2.2 Experimental procedure

2.2.1 Mechanical testing

Tensile tests

Tensile tests were conducted in displacement-controlled mode (2 mm/min) at room temperature using a 100kN capacity load cell of a MTS electro-mechanical testing machine. These conditions insure a quasi-static loading with a strain rate of about 10^{-3} s^{-1}. The axial strain was measured by means of a blade extensometer whose gage length is 12mm. The dimensions of the tensile specimens are specified in Fig. 2a. According the build direction, three types of tensile specimens (A, B and C) were machined to evaluate the influence of the AM process on the tensile properties (Fig. 2b). The anisotropy of cast samples has not been

studied by mechanical testing in different directions as cast specimens were machined from as-received round bars.

Single-edge-notch bending tests

SENB tests (Fig. 3) were performed at room temperature using a 100kN capacity load cell of an MTS 810 servo-hydraulic testing machine in quasi-static displacement-controlled mode (1mm/min). The mechanical properties in bending (modulus, strain and stress) were determined according to the following relationships:

$$\varepsilon_{bending} = \frac{6dw}{s^2} \quad \text{and} \quad \sigma_{bending} = \frac{3Ps}{2bw^2} \tag{1}$$

Where b is specimen's thickness, s is the span between the support points, and d is the displacement applied to the upper part of the specimen (Fig. 3).

2.2.2 Fracture toughness estimation

Inconel 718 alloys have a very ductile behavior [5-6]. To assess the structural integrity of the material in the presence of preexisting defects, it is necessary to quantify their fracture behavior by means of the *J*-integral vs. crack growth resistance (*J*-*R*) curve [1-3]. These curves represent the energy per unit of fracture area required to initiate and propagate the crack. The value of the fracture toughness at the initiation is called J_{Ic}. This value is associated with the mechanical energy required for the fracture to occur in the material [7]. The procedure for obtaining the *J*-*R* curve is described in ASTM E1820-01 standard test method. Depending on the fracture mode, this standard recommends the use of specimens with different geometries on which are machined notches for stress concentration and crack initiation purposes. Thus, fracture toughness tests were conducted on SENB specimens whose dimensions are given in Fig. 1. In order to estimate the influence of possible anisotropy induced by PBF process on the fracture behavior, notches were machined with different plane

orientations with respect to the lasing planes (Fig. 4). Three specimens were tested in each AM material type and four in cast material.

In materials with ductile fracture behaviors, the mode I fracture toughness J_I is computed from the elastic-plastic fracture mechanics concepts proposed by [43-46] :

$$J_I = J_{elastic} + J_{plastic} \tag{2}$$

With $J_{elastic}$ computed from the mode I critical stress intensity factor K_{Ic} [47] and the elastic constants of the materials (Young modulus E and Poisson ratio ν):

$$J_{elastic} = \frac{K_{Ic}^2(1-\nu^2)}{E} \tag{3}$$

And the plastic component $J_{plastic}$ is obtained from the mechanical energy dissipated A_{pl} corresponding to the area under the force-displacement curve:

$$J_{plastic\,(i)} = \left[J_{plastic\,(i-1)} + \frac{\eta_{pl\,(i-1)}}{b_{(i-1)}}\left(\frac{A_{pl\,(i)} - A_{pl\,(i-1)}}{B_N}\right)\right].\left[1 - \gamma_{pl\,(i-1)}\left(\frac{a_{(i)} - a_{(i-1)}}{b_{(i-1)}}\right)\right] \tag{4}$$

where $\eta_{pl\,(i-1)} = 1.9$ and $\gamma_{pl\,(i-1)} = 0.9$ are plastic factors in agreement with ASTM E1820 standard test method in the case of SEN specimens loaded in bending. . B_N is the net specimen thickness. $a_{(i)}$ and $b_{(i)} = w - a_{(i)}$ are the crack length and the unbroken ligament at iteration (i), respectively. These values are computed for each iteration (i) by means of the experimental data obtained from the digital image analysis detailed in the section 2.2.3.

In notched specimens, the triaxiality factor TF is defined from the mean stress $\sigma_m = 1/3\,(\sigma_1 + \sigma_2 + \sigma_3)$ and the equivalent Von Mises stress $\bar{\sigma}$ as follows:

$$TF = \frac{\sigma_m}{\bar{\sigma}} \tag{5}$$

2.2.3 In situ location of the crack tip

A high-speed monochrome Grasshopper® camera was used to record digital images of the outer surface during thermomechanical loading. By means of an algorithm based on a

binarization method and implemented in the free source numerical computation software Scilab, digital images were thresholded in order to track the location of the crack tip during mechanical loading. To know the position of crack tip, images are computed by the algorithm from top to bottom in search of a pixel value change, therefore indicating the crack tip. The physical meaning of the crack tip is also verified by comparing its location between two successive images (Fig. 5).

2.2.4 Microstructure characterization and fractographic analyses

The microstructure was characterized by means of a Keyence VHX-1000 digital microscope and a JEOL 7900F Scanning Electron Microscopy (SEM) coupled with Electron BackScattered Diffraction (EBSD). For all microstructure observations, acquisitions were done using EDAX OIM analysis software with a 0.7 µm step on samples electro-polished with an A2 solution at 24V for 30 seconds (Struers Lectropol-5). For melting pools characterization, chemical attack was performed at 10V during 5 seconds using the same electrolyte. Fracture mechanisms were analyzed and discussed by means of microscopic (Optical and SEM) observations.

3. Results and discussion

3.1 EBSD microstructure analyses

The microstructure was investigated by SEM-EBSD to reveal the grains crystallography and grain morphology. Fig. 6a-c-d display the inverse pole figure (IPF) of normal direction XY, YZ and XZ planes for PBF samples, as described in Fig. 2b. The IPF map of the cast sample is shown in Fig. 6b for comparison. EBSD results from these maps are summarized in Tab. 5. The XY and YZ/XZ EBSD maps reveal an anisotropy on the grain's morphology of PBF samples. For the XY map, the individual laser scan tracks are identified within many single tracks, and the width of the tracks was measured to be about 100 µm. This corresponds to the

hatch distance applied during the process. The laser scan tracks were composed of small equiaxed grains and inter-tracks large grains causing a large grain size distribution (cf. insert in Fig 6a). For the cross-section maps parallel to the building direction (YZ and XZ), the microstructure was dominated by cellular dentrites elongated along the building direction. It causes a grain shape aspect ratio lower than that measured in (XY) plane. Grains were longer than the layer thickness and pool depth resulting from an epitaxial growth occurring during the PBF process. As shown in Tab. 5, the maximum of pole figure <5 implies a random texture of PBF samples and the low value of the Grain Orientation Spread parameter (GOS), indicated homogenous grain orientation for these samples.

In literature, similar microstructure has been observed for the PBF IN718 [22][48-49]; however, these samples are often textured. Here, the low texture observed may result from the chosen scanning strategy (67°) [50]. In Fig. 6b, the microstructure of cast sample presents an equiaxed grains with some annealing twins, typical for Ni-based superalloys [51-53]. The presence of these twins affects the aspect ratio value for cast sample (cf. Tab. 5). Similar average grain size range (20-40 µm) is found for both cast and PBF samples. A homogeneous texture can also be observed in cast samples. But the GOS value is higher than that of PBF samples revealing partial microstructure recovery. As shown in Fig. 2b and Fig. 6, microstructures of Type A (YZ) and Type B (XZ) samples with respect to the loading direction are different. There is a rotation angle of 90° of the elongated grains, where the loading is perpendicular and parallel to the building direction for samples A and B, respectively.

3.2 Mechanical behaviour

3.2.1 Monotonic tensile tests

From the macroscopic standpoint, all specimens are characterized by an elastic-ductile behavior (see Fig. 7). The tensile response of AM specimens is similar, but cast specimens are

much more ductile with an elongation at break (about 40%, cf. Tab. 6). This is virtually 50% higher than the value observed in AM specimens, suggesting that AM significantly modifies plastic deformation mechanisms. From the tensile properties standpoint, type C specimens significantly differ from other specimens as their yield and ultimate tensile strengths are 20% and 10% lower, respectively (Tab. 6). As far the axial stiffness is concerned, there are significant differences between the AM specimens as type C value is 1.5 times that of type A for which the average value is similar to the one of cast specimens. This result suggests that lasing planes are somehow equivalent to a laminated material such as the formation of columnar grains through the sample thickness (Fig. 6c) may provide good adhesion between the layers. Ultimately, it may contribute to a significant improvement of the axial stiffness with respect to other AM specimens.

3.2.2 SENB tests

From the definitions given in Eq. (1), the bending stress-strain curves are drawn from load-displacement data. These curves clearly imply that both cast and AM specimens are characterized by large plastic deformations (up to about 6%) followed by ductile fracture behaviors (Fig. 8). The manufacturing process significantly influences the mechanical behavior (plasticity and fracture) of Inconel 718 Single Edge Notch specimens subjected to bending loading at ambient temperature. With respect to cast specimens, both yield and maximum strengths of AM specimens decrease (see Tab. 7) whereas the maximum strain is much higher (Fig. 8).

It is worth noticing that cast specimens reach ultimate failure. This is not observed in AM samples at the end of test. In type A specimens, the decrease in yield and maximum strengths is about -24% and -13%, respectively. In type B specimens, though a more significant dispersion of experimental data is observed, the decrease is about -8% and -10%, respectively. The decrease in yield strength and the increase in maximum strain observed in AM samples

suggest that plastic deformation mechanisms are more extensive in these samples. It also indicates that ductility will be play a prominent role into the fracture initiation and propagation as pointed out in Fig. 8. Initiation point is determined from the surface crack onset based on the examination of digital pictures. In addition, displacement-controlled mechanical tests imply that the crack initiation starts slightly earlier in cast specimens. This feature seems to indicate that earlier local plastic deformation (resulting from lower yield strength) near the crack tip may contribute to delaying the onset of the crack.

The crack propagations also differ between the cast and AM specimens (Fig. 9). Indeed, the rate of cracking appears to be steady until ultimate failure in cast samples (at about 6mm of transverse displacement). Nevertheless, it is slightly slower and gradually decreases from an applied displacement of about 6mm in AM specimens. These observations also suggest that more extensive plastic deformation mechanisms will take place within these specimens, therefore resulting in slowing down the crack growth. Finally, the value of the crack length is slightly lower in AM specimens in which the ultimate failure is not observed at the end of the bending test.

3.3 Evaluation of the fracture toughness

As far fracture toughness and behavior are concerned, the notches plane orientations with respect to the lasing planes (Fig. 4) are expected to have a significant influence resulting from the anisotropy induced by the additive manufacturing process (Fig. 10).

As indicated in the previous section, all specimens experience ductile fracture with a slow crack growth. The description of ductile fracture behaviour is classically based on the *J-R* curves. These curves require the evaluation of the fracture energy (or strain energy release rate) denoted by $J = J_{elastic} + J_{plastic}$ and the crack extension Δa along with the mechanical loading. The strain energy release rate J is computed from Eqs 3-5 and the experimental data

resulting from SENB tests. The estimation of crack length is obtained from the *in situ* location of the crack tip by means of the optical-based technic described in section 2.2.

In materials characterized by a ductile fracture, *J-R* curves are typically characterized by successive deformation mechanisms: crack blunting then stable plastic tearing. Crack blunting results from the dissipation of mechanical energy resulting from plastic deformation mechanisms near crack tip when crack initiates. In the early stage of loading, crack blunting is primarily observed at specimen surface where the triaxiality factor is low what facilitates local plastic deformations. It therefore causes the formation of a deformed area prior to material separation. While the lips of the initial notch open along with plasticity, the energy required by the crack to propagate increases. Usually, crack blunting is characterized by a momentary steep increase in the value of J with little crack growth. The *J-R* curves are different depending on the manufacturing process from which the specimens are obtained (Fig. 11). Crack blunting is clearly observed in cast specimens with two different slopes in *J-R* curves, but not in AM specimens. This observation is rather unexpected as the yield strength of AM specimens is lower (-10 to 24%) with respect to cast specimens. It therefore suggests that early plastic deformations do not promote extensive plasticity near the crack tip. It also indicates that the onset of plastic mechanisms within the materials does not necessarily mean lower fracture toughness at initiation. Finally, the slope of AM specimens *J-R* curves is steady and virtually the same as the one of cast specimens during the stable ductile tearing phase.

As commented previously when discussing the mechanisms of crack blunting, another major difference between cast and AM specimens is the value of fracture toughness at crack initiation (Fig. 12). This value is deduced from the value of the strain energy release rate when crack length starts growing. It clearly appears that fracture toughness at crack initiation significantly increases in AM specimens, as their value is about 70% and 100% higher, in types A and B specimens, respectively. The question is therefore to know why fracture toughness at initiation is higher in AM specimens.

These previous results tend to illustrate that cast and AM specimen fracture behaviour primarily differ in the early stage of fracture resulting from different fracture mechanisms. These mechanisms are addressed by means of fractographic analyses based on macroscopic (Optical) and SEM observations of fracture surfaces. They also result from specific microstructure features that will be further investigated in the section 3.4.

3.4 Fractographic analyses

Three point bending loading conditions applied to SEN specimens are expected to cause a mode I fracture mechanism. Even for pure mode I macroscopic loading, local mixed-mode (I and III modes) is observed depending on material ductility or specimen thickness [54-55]. To evaluate the influence of microstructure (depending on manufacturing process and heat treatments) on fracture mechanisms, fractographic analyses were conducted at macroscopic scale via digital microscope observations, and at microscopic scale via SEM observations.

3.4.1 Macroscopic observations of fracture surfaces

As expected, the macroscopic observations of fracture surfaces are relevant to draw conclusions on both the fracture modes and the corresponding fracture energies which are associated with fracture toughness. All Inconel specimens are characterized by ductile fracture behaviors. In specimen core, the fracture surface is primary flat (plane strain conditions). On the outer surfaces of specimens, fracture surfaces form shear lips resulting from a ductile mixed mode failure [56]. The material is in state of plane stresses, plastic deformation mechanisms occur by shearing along the 45° direction towards the lateral surface (Fig. 13). In addition, shear lips open freely on the surface. Plasticity is prominent near the outer surfaces where the triaxiality factor remains low. The shear lips are not very large in cast and type B specimens. The ratio of flat surface over lips surface is a rough approximate of the differences in triaxiality factors between tested materials. This ratio is higher (about 2.3) in cast and type

B specimens with respect to type A specimens (about 1.5). These results suggest that the failure modes differ from one manufacturing process to another. In all specimens tested, the ductile fracture processes either occur in mode I (specimen core) or mixed-mode (outer surfaces) depending on the triaxiality rate. The critical fracture energy J_c is low in specimen core (which is in plane strain state); however, the fracture energy is much higher in the shear lips (which are in plane stresses states) because plasticity is more extensive on the outer free surfaces. The fracture energy is therefore minimal in plane strain and is called the critical fracture toughness in mode I (denoted J_{Ic}). It is independent from specimen thickness as it is sufficient for the plane strain state to be achieved. J_{Ic} is therefore an intrinsic characteristic of the material. When the shear lips are large (type B specimen), the mixed-mode fracture requires more mechanical energy to be dissipated than the energy required in mode I fracture. Hence, the corresponding fracture toughness is expected to be higher in type B specimens. In cast and type A specimens, the shear lips are confined in the vicinity of the outer surfaces (Fig. 14a and 14b). Fracture primarily occurs in mode I and the fracture energy is referred to as J_{Ic}. In type B specimens, the shear lips in plane stress occupy an important part of the fracture surface (Fig. 14c). This is the same effect as that observed when specimen thickness decreases. It therefore suggests that the position of the lasing planes perpendicular to the initial machined notch contribute to the increase in the fracture energy resulting from mode I (specimen core) and mixed-mode fractures. In addition to the macroscopic observations of fracture surfaces from different point of view, the influence of the manufacturing process is also clearly noticeable when considering the surface crack paths. The crack path is obtained from the digital image analysis (described in section 2.2.4). This allows the *in situ* location of the crack tip during the mechanical loading (Fig. 15). In cast specimens, crack growth is primarily driven by a mode I fracture as the crack virtually remains in the initial notch plane what is also known as self-similar fracture. In AM specimens, the crack path on the outer

surface does not remain in the initial notch plane (also known as non-self-similar), therefore confirming a mixed-mode failure mode.

3.4.2 Microscopic observations of fracture surfaces

SEM observations provide insights into the influence of the manufacturing process on the mechanisms associated with crack growth at microscopic scale (Fig. 16). The fracture surfaces of cast and additively manufactured specimens present a dimpled surface. This is a feature of a transgranular ductile failure mode. Dimples result from the debonding between the f.c.c. matrix and the secondary phase inclusions. It appears that the size of the dimples significantly depends on the triaxiality factor. Thus, the SEM observations of flat surfaces (high triaxiality factor) in Inconel 718 SENB specimens imply dimples with similar size in all specimens (Fig. 17); however, the SEM observations of shear lips (low triaxiality factor) present dimples only in cast specimens (Fig. 16). In AM specimens, extensive channel fracture (striations) surrounding small primary dimples with large walls are observed along with secondary cracks (Fig. 17b and 17c). Striations are marks produced on the fracture surface that reveal the incremental growth of cracks. Striations are more specific to AM specimens and their formation may result in delaying the advance of the crack front, hence causing higher fracture toughness with respect to cast specimens. SEM observations of the core area at high magnification (x1000) also reveal that fracture surfaces are characterized by micro-voids nucleated at the inclusions (Fig. 18). Micro-voids coalescence is usually observed in materials experiencing a ductile fracture mode.

In cast specimens, the fracture process involves the formation of primary microvoids at failed inclusions (Fig. 18a). Subsequent separation of the ligaments between primary micro-voids then caused the crack front growth. As pointed out by Mills et al, ligament separation in the cast specimens involved three possible mechanisms: coalescence of micro-voids, void sheet formation initiated by the y'' phase, and channel fracture whereby localized tearing occurred

along planar slip bands [1]. The latter two mechanisms usually occur during the final stages of fracture as primary micro-voids were about to impinge; hence, they did not necessarily degrade fracture resistance. As indicated by the macroscopic observations of fracture surfaces (previous section), the failure mode is usually referred to as mode I fracture in cast specimens. It is dominated by void initiation occurring at a second phase particle or inclusions, and followed by void growth in the crack plane. SEM observations at higher magnification reveal that fracture surfaces consist of small dimples each being nucleated at a precipitate whose size and shape are typical of the δ Laves phases as commonly observed in the literature [5]. Indeed, the primary fracture mechanism is a slow tearing process within large pockets of inhomogeneous carbides and nitrides. In cast specimens, this fracture is associated with fracture toughness values ranging from about 400kJ/m² at initiation to values of about 810kJ/m² at ultimate failure. As pointed out by many authors, the fracture mechanism involves fracture initiation at carbides and nitrides followed by off crack plane void sheet growth nucleated at the Laves intermetallic phases [1][5][15].

In AM specimens, SEM observations with high magnification of core fracture surfaces also reveal micro-voids coalescence and a large number of dimples. These features are representative of a transgranular failure mode [37]. A few cracks may initiate from process-induced porosities. SEM observations also suggest that the growth of the cracks initiated from the secondary phases may be delayed by the presence of striations (Fig. 18b). Indeed, the dimples are characterized by large walls as forming striations. The formation of these striations is commonly observed in specimens subjected to fatigue loadings resulting from the incremental crack growth. These striations interact with the secondary phases in the interdendritic regions [37]. In cast specimens, due to the inhomogeneous deformation between the austenitic matrix and the secondary phases, these phases are preferential sites for cracks nucleation (Fig. 18a).

Finally, the coarse grain microstructure of AM specimens is characterized by columnar grains (Fig. 6) resulting in intergranular fracture with secondary cracks initiating at the grain boundaries [34]. In AM specimens, depending on the location of the initial notch with respect to the lasing planes, the energy required to initiate cracking from secondary phases ranges from 666-790kJ/m² in type A and B specimens. The energy required to grow cracks until ultimate failure is about 750kJ/m² and 936kJ/m² in type A and type B specimens, respectively. The presence of secondary cracks on core fracture surfaces (Fig. 17) may result from the different crystallographic textures (Fig. 6) or from higher triaxiality factors in AM specimens associated with the spatial distribution of lasing planes [57]. In other words, the formation of secondary cracks could be fostered between lasing tracks. The presence of these secondary cracks may also dissipate the mechanical energy, hence contributing to the increase in the fracture toughness in AM specimens. In type B specimens, the crack growth through two successive layers (or lasing planes – see Fig. 10) is expected to be more difficult to propagate than in type A specimens in which the crack propagates more easily at the interface between two layers. As a result, the mechanisms responsible for these crack growths may reflect on the fracture toughness and explain why higher values are observed in type B specimens.

4. Conclusion

The influence of manufacturing processes (cast and additive manufacturing) on the microstructure and mechanical behavior of Inconel 718 alloys is addressed. The tensile behavior and the ductile fracture were investigated along with their underlying deformation and damage mechanisms. A few major conclusions are drawn from this study:

- Without heat treatment, cast and AM specimens have different microstructures. Cast specimens are characterized by significant grain disorientations whereas AM samples imply a morphological texture.

- Significant changes in axial stiffness suggest that lasing planes are equivalent to a laminated material such as the formation of columnar grains through the sample thickness may provide good adhesion between the layers.
- All specimens experience a transgranular ductile fracture at macroscopic scale, and the analysis of fracture surfaces reveal different fracture mechanisms at microscopic scale.
- With respect to cast specimens, the critical fracture toughness (at crack initiation) of AM specimens is about 70% and 100% higher, in types A and B specimens, respectively.
- AM specimens do not experience a purely mode I fracture contrary to cast specimens. They are characterized by curved crack paths, resulting in larger fracture surfaces. These differences may explain why AM specimens have much higher fracture toughness at initiation.
- The J-R curves, obtained from the ASTM standard E1820-01, are different depending on the manufacturing process. Once the crack is initiated, the energy required to grow the crack, during the stable ductile tearing phase, is the same in all specimens.
- Due to different microstructures and depending on the location of the initial notch with respect to the lasing planes, the crack growth through two successive lasing planes (type B specimen) is more difficult to propagate than in type A specimens in which the crack propagates more easily at the interface between two layers. As a result, the mechanisms responsible for these crack growths may reflect on the fracture toughness and explain why higher values are observed in type B specimens.

In a forthcoming paper, the influence of testing temperature on the fracture toughness properties of cast and AM Inconel alloy 718 will be investigated.

References

[1] W. J. Mills, L. D. Blackburn. Variations in Fracture Toughness for Alloy 718 Given a Modified Heat Treatment. Transactions of the ASME, 1990; 112: 116-123.

[2] W.J. Mills. The Deformation and Fracture Characteristics of Inconel X-750 at Room Temperature and Elevated Temperatures. Metallurgical Transactions, 1980; 11A:1039-1047.

[3] W.J. Mills. Fracture toughness variations for alloy 718 base metal and welds. Superalloy 718-Metallurgy and Applications Edited by E.A. Loria The Minerals, Metals 8 Materials Society, 1989.

[4] Pettit, D. E., Feddersen, C. E., Mindlin, H. Flaw Growth Behavior of Inconel 718 at Room and Cryogenic Temperatures, NASA Report CR-101942, Battelle-Columbus Laboratories, Columbus, OH, 1969.

[5] M.G. Stout, W.W. Gerberich. Structural Property/Continuum Synthesis of Ductile Fracture in Inconel 718. Metallurgical Transactions 1978; 9A:649-658.

[6] B.H. Menke, F.L. Loss, J.R. Hawthorne. An Elastic-Plastic Toughness Characterization of Alloy 718 Product Forms, NRL Memorandum Report 4403, Naval Research Laboratory, Washington, DC, Jan. 1981.

[7] J.A. Begley, J.D. Landes. "The J Integral as a Fracture Criterion," Fracture Toughness, ASTM-STP 514, American Society for Testing and Materials, Philadelphia, PA, 1974, pp. 1-20.

[8] R.O. Ritchie, A.W. Thompson. Macroscopic and Microscopic Analyses for Crack Initiation and Crack Growth Toughness in Ductile Alloys, Metallurgical Transaction 1985; 16A:233-248.

[9] D. Gustafsson, J. Moverare, S. Johansson, M. Hörnqvist, K. Simonsson, S. Sjöström, B. Sharifimajda. Fatigue crack growth behaviour of Inconel 718 with high temperature hold times. Procedia Engineering 2010; 2:1095–1104.

[10] Y. Zhang, M. Bellet, G. Guillemot, C-A. Gandin. Macroscopic finite element thermal modelling of laser beam melting of Inconel 718. 1st Int. Congress on Welding and Additive Manufacturing and associated nondestructive testing (ICWAM), May 2017, Metz, France.

[11] L.N. Carter, C. Martin, P.J. Withers, M.M. Attallah. The influence of the laser scan strategy on grain structure and cracking behaviour in PBF powder-bed fabricated nickel superalloy. Journal of Alloys and Compounds 2014; 615: 338-347.

[12] T. Debroy, H.L. Wei, J.S. Zuback, T. Mukherjee, J.W. Elmer, J.O. Milewski, A.M. Beese, A. Wilson-Heid, A. De, W. Zhang. Additive manufacturing of metallic components – Process, structure and properties. Progress in Materials Science 2018; 92: 112-224.

[13] J.J. Lewandowski, M. Seifi. Metal Additive Manufacturing: A Review of Mechanical Properties. Annu. Rev. Mater. Res. 2016; 46:151–86.

[14] Y.N. Zhang, X. Cao, P. Wanjara, M. Medraj. Tensile properties of laser additive manufactured Inconel 718 using filler wire. Journal of Materials Research 2014 ; 29(17):2006-2020.

[15] D. Zhang, Z. Feng, C. Wang, W. Wang, Z. Liu, W. Niu. Comparison of microstructures and mechanical properties of Inconel 718 alloy processed by selective laser melting and casting, Materials Science and Engineering: A 2018; 724: 357-367.

[16] J. Li, Z. Zhao, P. Bai, H. Qu, B. Liu, L. Li, L. Wu, R. Guan, H. Liu, Z. Guo. Microstructural evolution and mechanical properties of IN718 alloy fabricated by selective laser melting following different heat treatments. Journal of Alloys and Compounds 2019; 772: 861-870.

[17] Z. Wang, K. Guan, M. Gao, X. Li, X. Chen, X. Zeng. The microstructure and mechanical properties of deposited-IN718 by selective laser melting. Journal of Alloys and Compounds 2012; 513: 518-523.

[18] T. Trosch, J. Strößner, R. Völkl, U. Glatzel. Microstructure and mechanical properties of selective laser melted Inconel 718 compared to forging and casting. Materials Letters 2016; 164: 428-431.

[19] S. Sui, J. Chen, E. Fan, H. Yang, X. Lin, W. Huang. The influence of Laves phases on the high-cycle fatigue behavior of laser additive manufactured Inconel 718. Materials Science and Engineering: A 2017; 695: 6-13.

[20] K. Moussaoui, W. Rubio, M. Mousseigne, T. Sultan, F. Rezai. Effects of Selective Laser Melting additive manufacturing parameters of Inconel 718 on porosity, microstructure and mechanical properties. Materials Science and Engineering: A 2018; 735: 182-190.

[21] J. Schneider, B. Lund, M. Fullen. Effect of heat treatment variations on the mechanical properties of Inconel 718 selective laser melted specimens. Additive Manufacturing 2018; 21: 248-254.

[22] S. Holland, X. Wang, J. Chen, W. Cai, F. Yan, L. Li. Multiscale characterization of microstructures and mechanical properties of Inconel 718 fabricated by selective laser melting, Journal of Alloys and Compounds 2019; 784: 182-194.

[23] K.N. Amato, S.M. Gaytan, L.E. Murr, E. Martinez, P.W. Shindo, J. Hernandez, S. Collins, F. Medina. Microstructures and mechanical behavior of Inconel 718 fabricated by selective laser melting. Acta Materialia 2012; 60(5): 2229-2239.

[24] E. Chlebus, K. Gruber, B. Kuźnicka, J. Kurzac, T. Kurzynowski. Effect of heat treatment on the microstructure and mechanical properties of Inconel 718 processed by selective laser melting. Materials Science and Engineering: A 2015; 639: 647-655.

[25] D. Deng, R.L. Peng, H. Brodin, J. Moverare. Microstructure and mechanical properties of Inconel 718 produced by selective laser melting: Sample orientation dependence and effects of post heat treatments. Materials Science and Engineering: A 2018; 713: 294-306.

[26] Q. Jia, D. Gu. Selective laser melting additive manufacturing of Inconel 718 superalloy parts: Densification, microstructure and properties. Journal of Alloys and Compounds 2014; 585: 713-721.

[27] W.M. Tucho, P. Cuvillier, A. Sjolyst-Kverneland, V. Hansen. Microstructure and hardness studies of Inconel 718 manufactured by selective laser melting before and after solution heat treatment. Materials Science and Engineering: A 2017; 689: 220-232.

[28] D. Zhang, W. Niu, X. Cao, Z. Liu. Effect of standard heat treatment on the microstructure and mechanical properties of selective laser melting manufactured Inconel 718 superalloy. Materials Science and Engineering: A 2015; 644: 32-40.

[29] T. Brynk, Z. Pakiela, K. Ludwichowska, B. Romelczyk, R.M. Molak, M. Plocinska, J. Kurzac, T. Kurzynowski, E. Chlebus. Fatigue crack growth rate and tensile strength of Re modified Inconel 718 produced by means of selective laser melting. Materials Science and Engineering: A 2017; 698: 289-301.

[30] G. Puppala, R. Kaul, C.P. Paul, P. Tiwari, S.K. Rai, R.C. Prasad, L.M. Kukreja. Fatigue and fracture toughness characteristics of laser rapid manufactured Inconel 625 structures. Materials Science and Engineering: A 2010; 527(29–30): 7490-7497.

[31] J.-R. Poulin, V. Brailovski, P. Terriault. Long fatigue crack propagation behavior of Inconel 625 processed by laser powder bed fusion: Influence of build orientation and post-processing conditions. International Journal of Fatigue 2018; 116: 634-647.

[32] R. Konečná, L. Kunz, G. Nicoletto, A. Bača. Long fatigue crack growth in Inconel 718 produced by selective laser melting. International Journal of Fatigue 2016; 92(2): 499-506.

[33] A. Riemer, H.A. Richard. Crack propagation in additive manufactured materials and structures.21st confrenece onf fracture ECF21, June 20-24 2016, Catania, Italy.

[34] V.A. Popovich, E.V. Borisov, V Heurtebise, T. Riemslag, A.A. Popovich, V.S. Sufiiarov. Creep and Thermomechanical Fatigue of Functionally Graded Inconel 718 Produced by Additive Manufacturing. In: & Materials Society T. (eds) TMS 2018 147th Annual Meeting &

Exhibition Supplemental Proceedings. TMS 2018. The Minerals, Metals & Materials Series. Springer, 2018.

[35] C. Pei, D. Shi, H. Yuan, H. Li. Assessment of mechanical properties and fatigue performance of a selective laser melted nickel-base superalloy Inconel 718. Materials Science and Engineering: A 2019; 759: 278-287.

[36] M.E. Aydinöz, F. Brenne, M. Schaper, C. Schaak, W. Tillmann, J. Nellesen, T. Niendorf. On the microstructural and mechanical properties of post-treated additively manufactured Inconel 718 superalloy under quasi-static and cyclic loading. Materials Science and Engineering: A 2016; 669: 246-258.

[37] H.Y. Wan, Z.J. Zhou, C.P. Li, G.F. Chen, G.P. Zhang. Effect of scanning strategy on mechanical properties of selective laser melted Inconel 718. Materials Science and Engineering: A 2019; 753: 42-48.

[38] O. Quénard, O. Dorival, P. Guy, A. Votié, K. Brethome. Measurement of fracture toughness of metallic materials produced by additive manufacturing. CEAS Space Journal 2018; 10(3): 343–353.

[39] G. Puppala, A. Moitra, S. Sathyanarayanan, R. Kaul, Sasikala G, R.C. Prasad, L.M. Kukreja. Evaluation of fracture toughness and impact toughness of laser rapid manufactured Inconel-625 structures and their co-relation. 13th International Conference on Fracture, June 16–21, 2013, Beijing, China.

[40] K. Solberg, F. Berto. Notch-defect interaction in additively manufactured Inconel 718. International Journal of Fatigue 2019; 122: 35-45.

[41]. A. Mostafa, I. Picazo Rubio, V. Brailovski, Mo. Jahazi, M. Medraj. Structure, texture and phases in 3D Printed IN718 Alloy Subjected to Homogenization and HIP Treatments. Metals 2017; 7, 196.

[42] ASTM E1820-01, Standard Test Method for Measurement of Fracture Toughness, ASTM International, West Conshohocken, PA, 2001.

[43] J.R. Rice, P.C. Paris, J.G. Merkle. Some further results of J-integral analysis and estimates. Progress in flaws growth and fracture toughness testing, ASTM STP 536. American Society for Testing and Materials 1973; 231–45.

[44] J.D.G. Sumpter, C.E. Turner. Method for laboratory determination of Jc. Cracks and fracture. ASTM STP 601. American Society for Testing and Materials 1976; 3–18.

[45] C.E. Turner. The ubiquitous η factor. In: Fracture mechanics: twelfth conference. ASTM STP 700. American Society for Testing and Materials 1980; 314–37.

[46] E. Roos, U. Eisele, H. Silcher. A procedure for the experimental assessment of the J-integral by means of specimen of different geometries. International Journal of Pressure Vessels and Piping 1986; 23:81–93.

[47] H. Tada, P.C. Paris, G.R. Irwin. The stress analysis of cracks handbook. ASME Press. Third Edition, January 2000.

[48] H.Y. Wan, Z.J. Zhou, C.P. Li, G.F. Chen, G.P. Zhang. Effect of scanning strategy on grain structure and crystallographic texture of Inconel 718 processed by selective laser melting. Journal of Materials Science & Technology 2018; 34(10): 1799-1804.

[49] J-P. Choi, G-H. Shin, S. Yang, D-Y. Yang, J-S. Lee, M. Brochu, J-H. Yu. Densification and microstructural investigation of Inconel 718 parts fabricated by selective laser melting. Powder Technology 2017; 310: 60-66.

[50] S-H. Sun, K. Hagihara, T. Nakano. Effect of scanning strategy on texture formation in Ni-25at.%Mo alloys fabricated by selective laser melting. Materials and Design 2018; 140: 307-316.

[51] H. Shi, K. Chen, Z. Shen, J. Wu, X. Dong, L. Zhang, A. Shan. Twin boundary characters established during dynamic recrystallization in a nickel alloy. Materials Characterization 2015; 110: 52-59.

[52] A. Mortezaie, M. Shamanian. An assessment of microstructure, mechanical properties and corrosion resistance of dissimilar welds between Inconel 718 and 310S austenitic stainless steel. International Journal of Pressure Vessels and Piping 2014; 116: 37-46.

[53] W-D. Song, M-L. Hu, H-S. Zhang, Y-X. Jin. Effects of different heat treatments on the dynamic shear response and shear localization in Inconel 718 alloy. Materials Science and Engineering: A 2018; 725: 76-87.

[54] Y. Madi, J. Besson, F. Tankoua, J. Chen, N. Recho. Mixed mode ductile fracture of an anisotropic 2024 Al-Cu alloy. Fracture of materials and structures from micro to macroscale - ECF 18, Aug 2010, Dresden, Germany.

[55] E. Mahgoub, X. Deng, M.A. Sutton. Three-dimensional stress and deformation fields around flat and slant cracks under remote Mode I loading conditions. Engineering Fracture Mechanics 2003; 70(18): 2527-2542.

[56] J. Belan, A. Vaško, L. Kuchariková, E. Tillová. The fractography analysis of IN718 alloy after three-point flexure fatigue test. MATEC Web of Conferences 157, 07001 (2018).

[57] M. Algarni, Y. Bai, Y. Choi. A study of Inconel 718 dependency on stress triaxiality and Lode angle in plastic deformation and ductile fracture. Engineering Fracture Mechanics 2015; 147: 140-157.

Figure captions

Fig. 1 – Single-edge-notch bending specimens for fracture toughness estimation – ASTM E1820-01 (dimensions are in mm)

Fig. 2 – Tensile test specimens: (a) Geometry – (b) AM samples with different orientations

Fig. 3 – SENB tests: dimensions and loading conditions in agreement with the ASTM E1820-01 standard test method [ASTM]

Fig. 4 – Configuration of notch plane with respect to lasing planes: (a) Type B – (b) Type A

Fig. 5 – Illustration of the *in situ* location of the crack tip location by means of a binarization method algorithm applied to digital image analysis

Fig. 6 – SEM-EBSD normal direction (ND) inverse pole figure (IPF) maps for samples elaborated by PBF (a, c, d). (b) Casting. (a, c, d) maps corresponds to plans XY, YZ and XZ, respectively. Black line corresponds to random grains boundaries. The insert corresponds to the grain size distribution.

Fig. 7 – Influence of the manufacturing process (cast or PBF AM) on the tensile behaviour: (a) early stage of the tensile loading – (b) macroscopic response

Fig. 8 – Macroscopic mechanical response of Inconel 718 Single Edge Notch specimens subjected to bending loading at ambient temperature:
(a) Cast – (b) Additively Manufactured (PBF)

Fig. 9 – Influence of the manufacturing process (cast or PBF additively manufactured) on the evolution of the crack length as a function of the applied displacement in Inconel 718 Single Edge Notch specimens subjected to bending loading at ambient temperature

Fig. 10 – Optical miscroscope observations of AM Inconel 718 blocks from which are machined the SENB specimens: (a) X-Y plane – (b) Building direction

Fig. 11 – Influence of the manufacturing process (cast or PBF additively manufactured) on the J-R curves representing the evolution of the fracture toughness as a function of the crack

length in Inconel 718 Single Edge Notch specimens subjected to bending loading at ambient temperature

Fig. 12 – Influence of the manufacturing process (cast or PBF additively manufactured) on the mode I fracture toughness at crack initiation in Inconel 718 Single Edge Notch specimens subjected to bending loading at ambient temperature

Fig. 13 – Side observations of fracture surface in SENB specimens: illustration of mixed-mode fracture

Fig. 14 – Fracture surfaces side observations of Inconel 718 SENB specimens:
(a) Cast – (b) Type A – (c) Type B

Fig. 15 – Influence of the manufacturing process (cast or PBF additively manufactured) on the crack path in Inconel 718 Single Edge Notch specimens subjected to bending loading at ambient temperature

Fig. 16 – SEM observations of shear lips fracture surfaces (low triaxiality factor) in Inconel 718 specimens presenting dimples only in cast specimens

Fig. 17 – SEM observations of core fracture surfaces (high triaxiality factor) in Inconel 718 specimens implying transgranular ductile failure mode (dimples). AM specimens are characterized by striations and secondary cracks (b-c)

Fig. 18 – SEM observations with high magnification of core fracture surfaces in Inconel 718 specimens implying micro-voids coalescence and dimples with large walls as well as striations in AM specimens J-R curves representing the evolution of the fracture toughness as a function of the crack

(a)

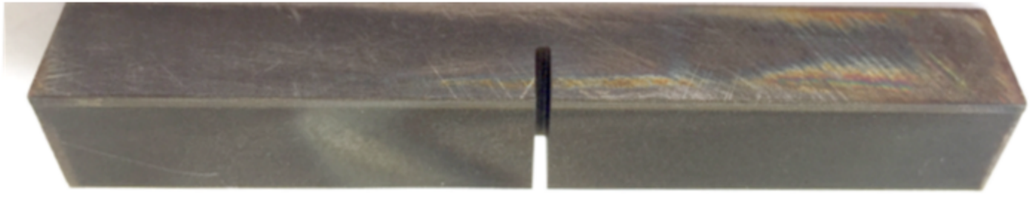

(b)

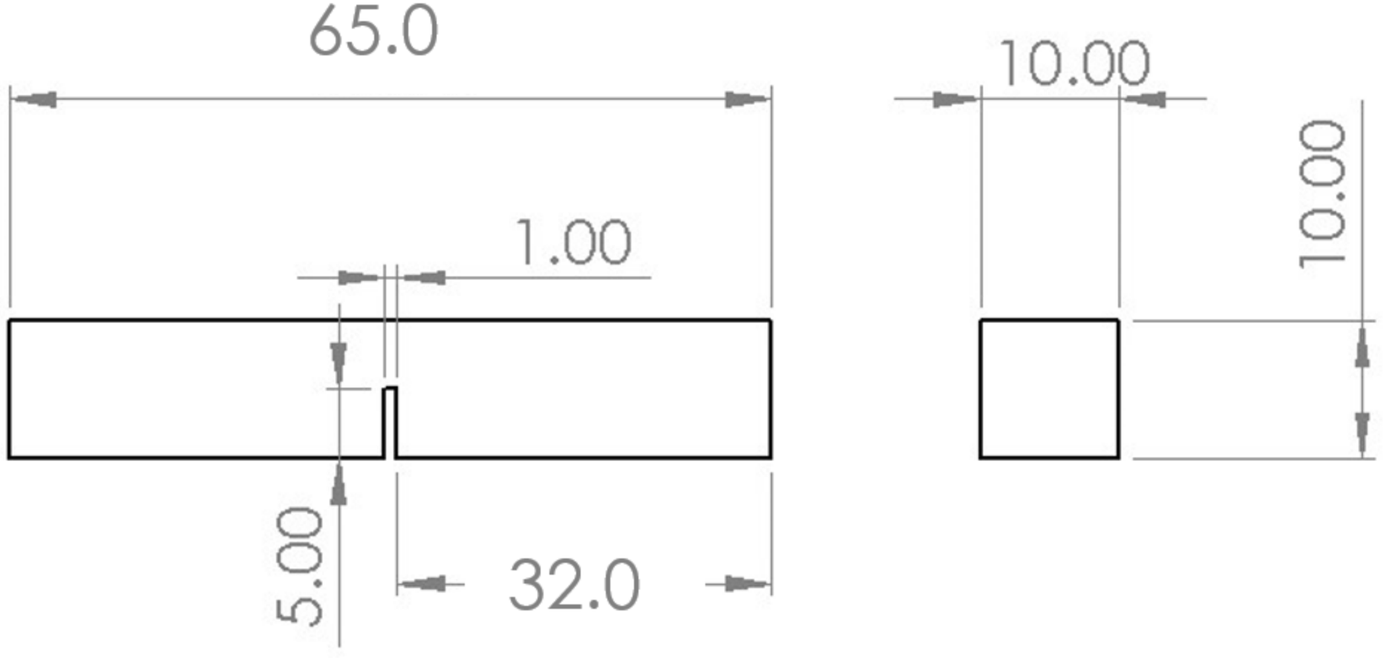

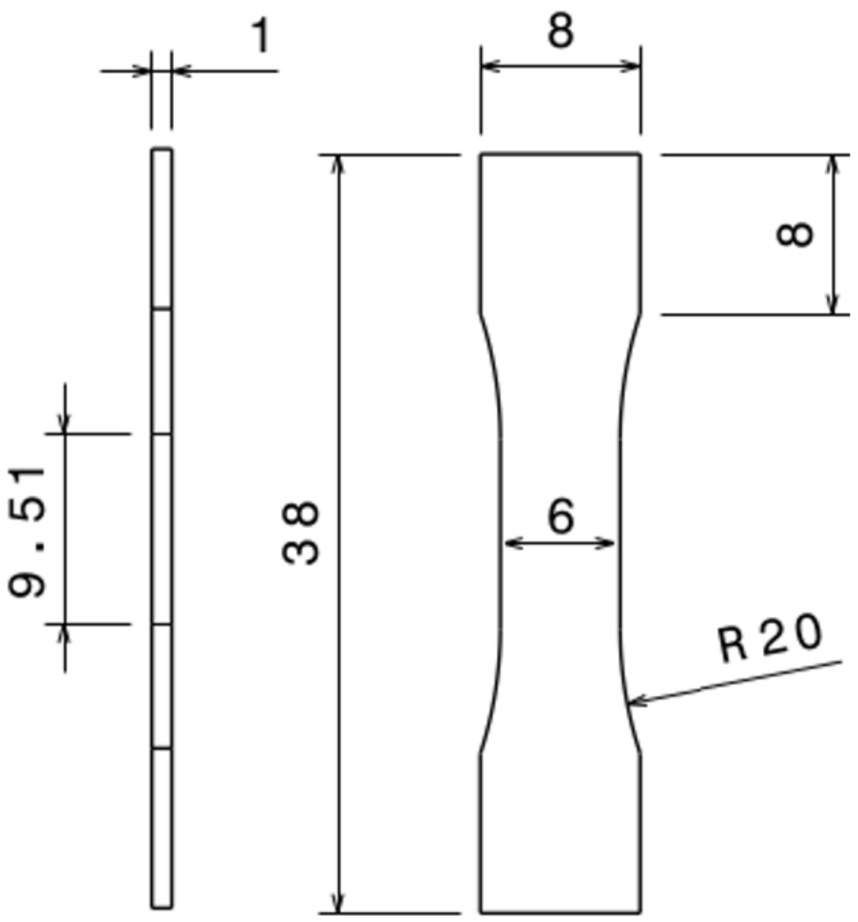
1
8
8
9.51
38
6
R 20

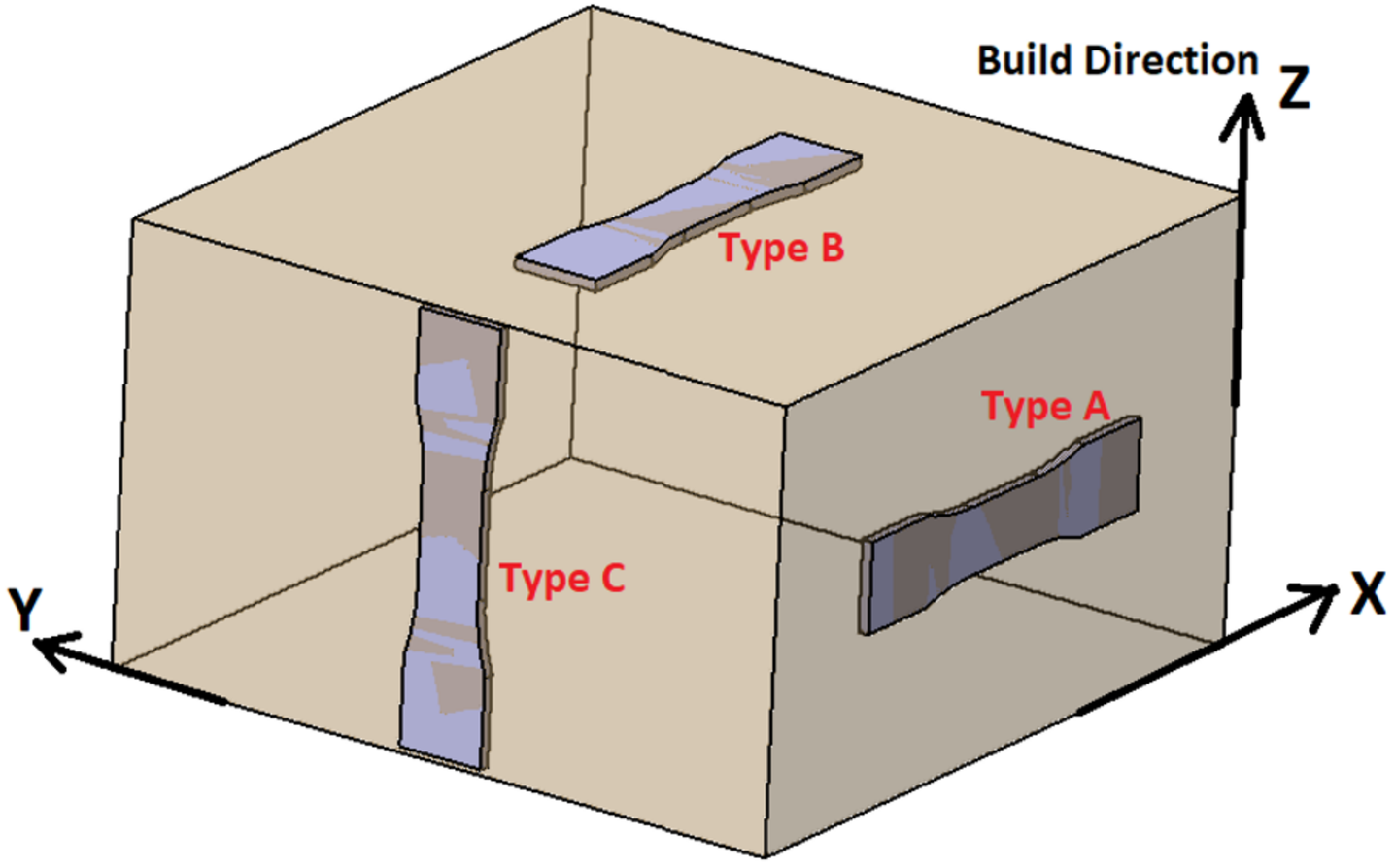
Build Direction
Z
Type B
Type A
Type C
Y
X

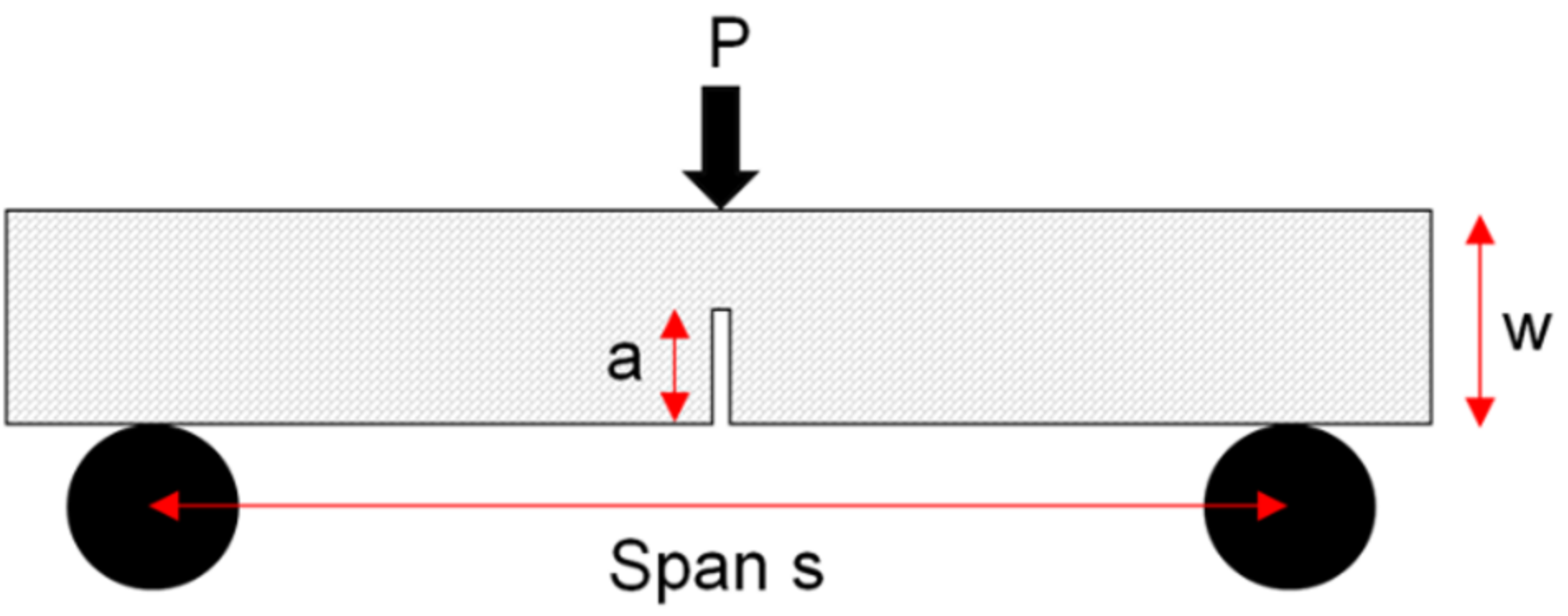
P
a
w
Span s

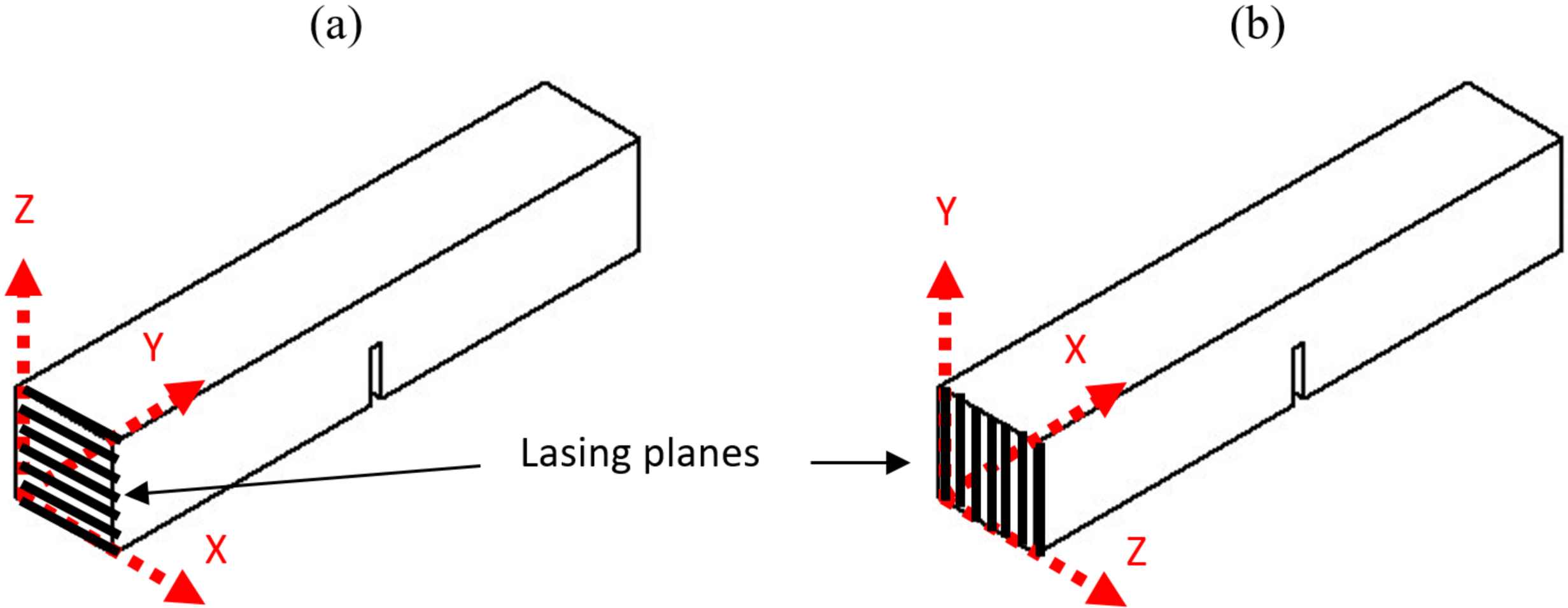
(a)
(b)
Z
Y
X
Lasing planes
Y
X
Z

(a)

(b)

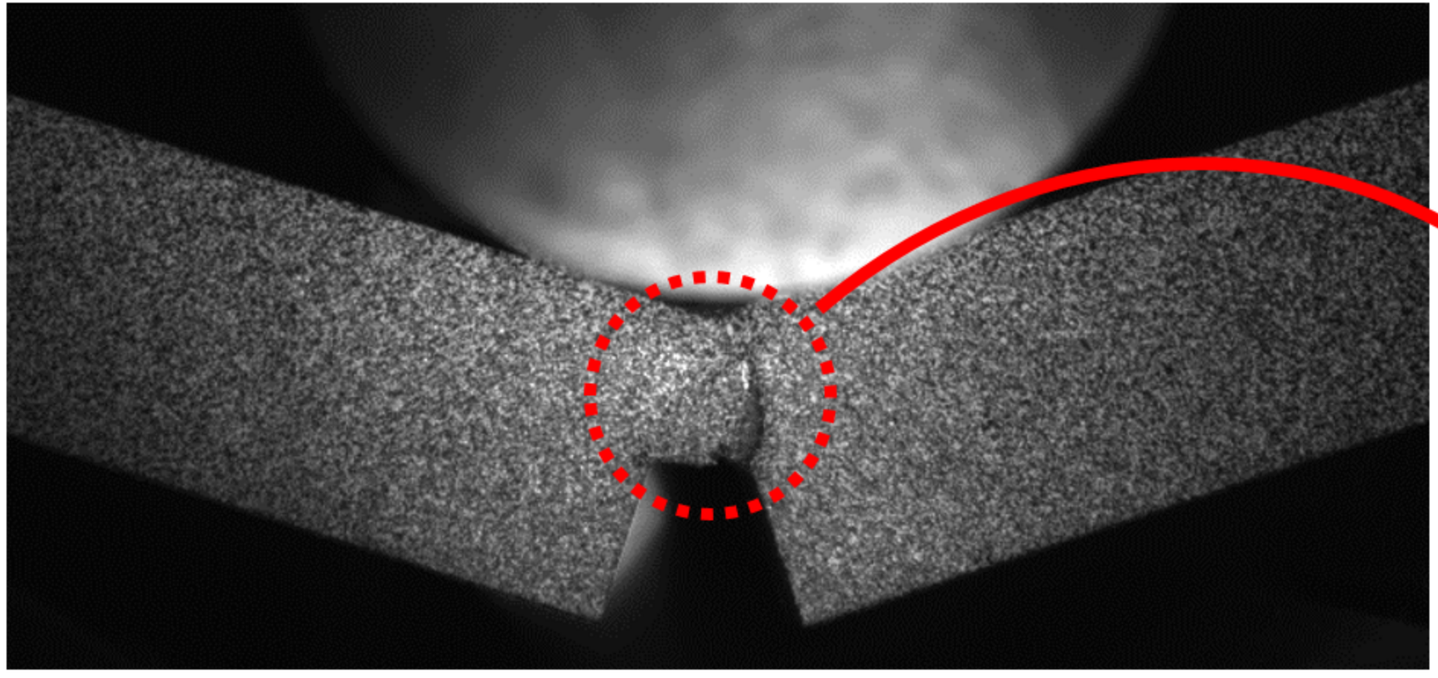

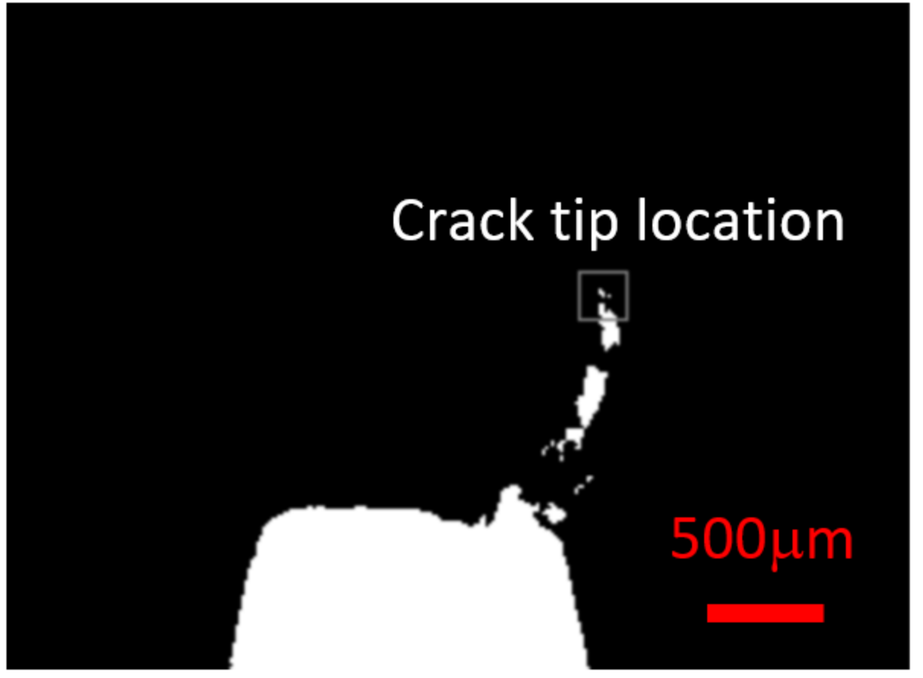

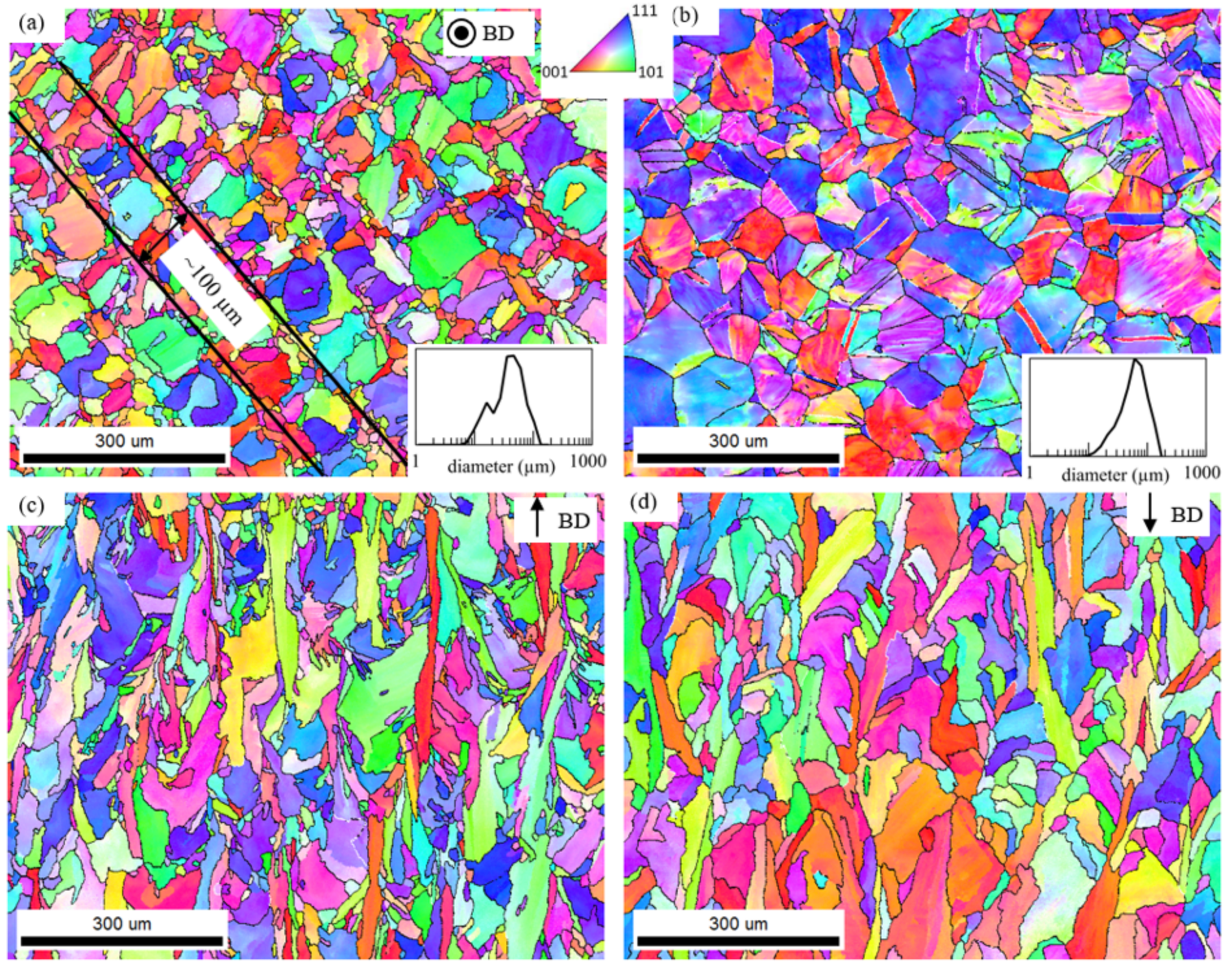
(a)
BD
111
001
101
~100 μm
300 um
1
diameter (μm)
1000
(b)
300 um
1
diameter (μm)
1000
(c)
BD
300 um
(d)
BD
300 um

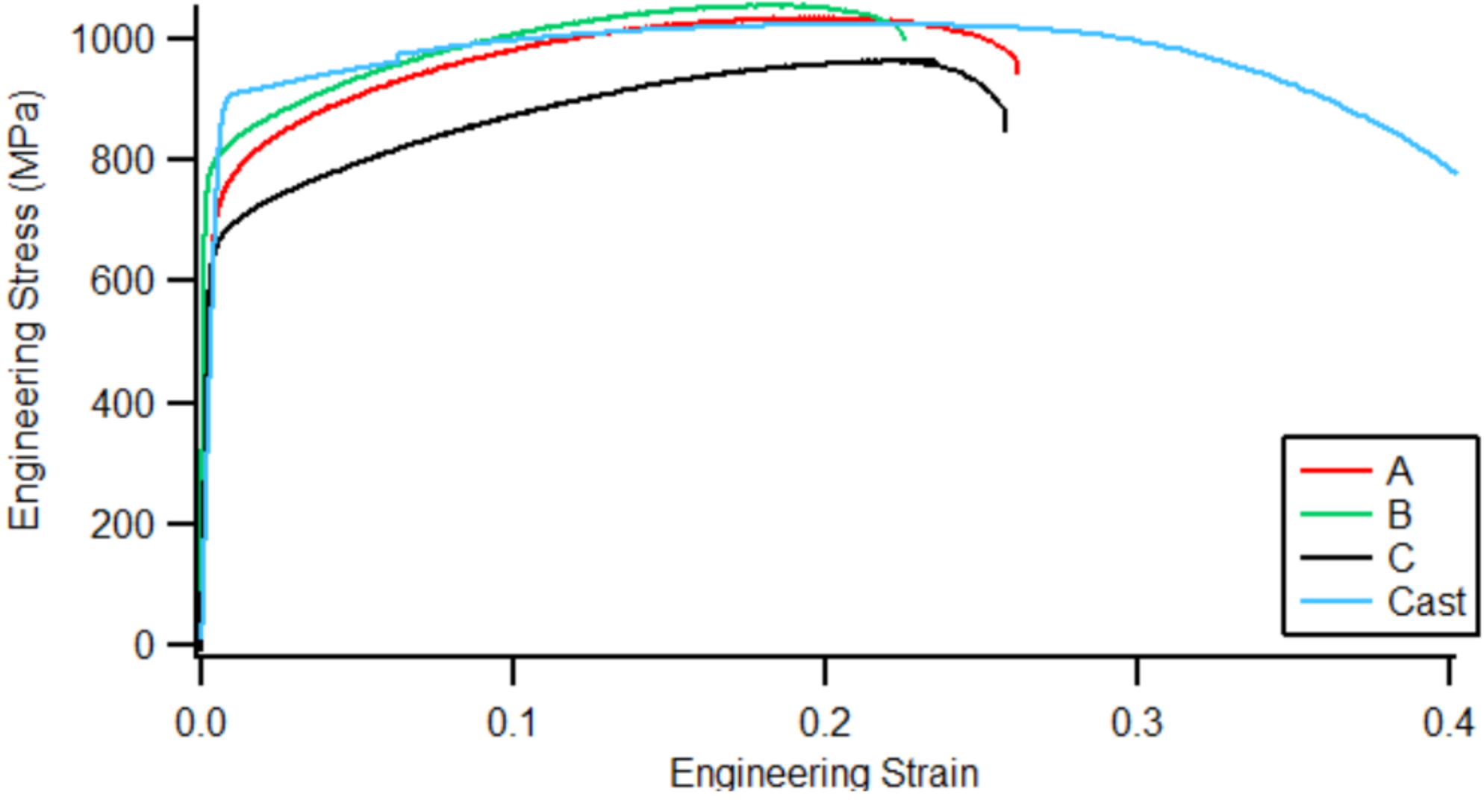
Engineering Stress (MPa)
1000
800
600
400
200
0
0.0
0.1
0.2
0.3
0.4
Engineering Strain
A
B
C
Cast

(a)

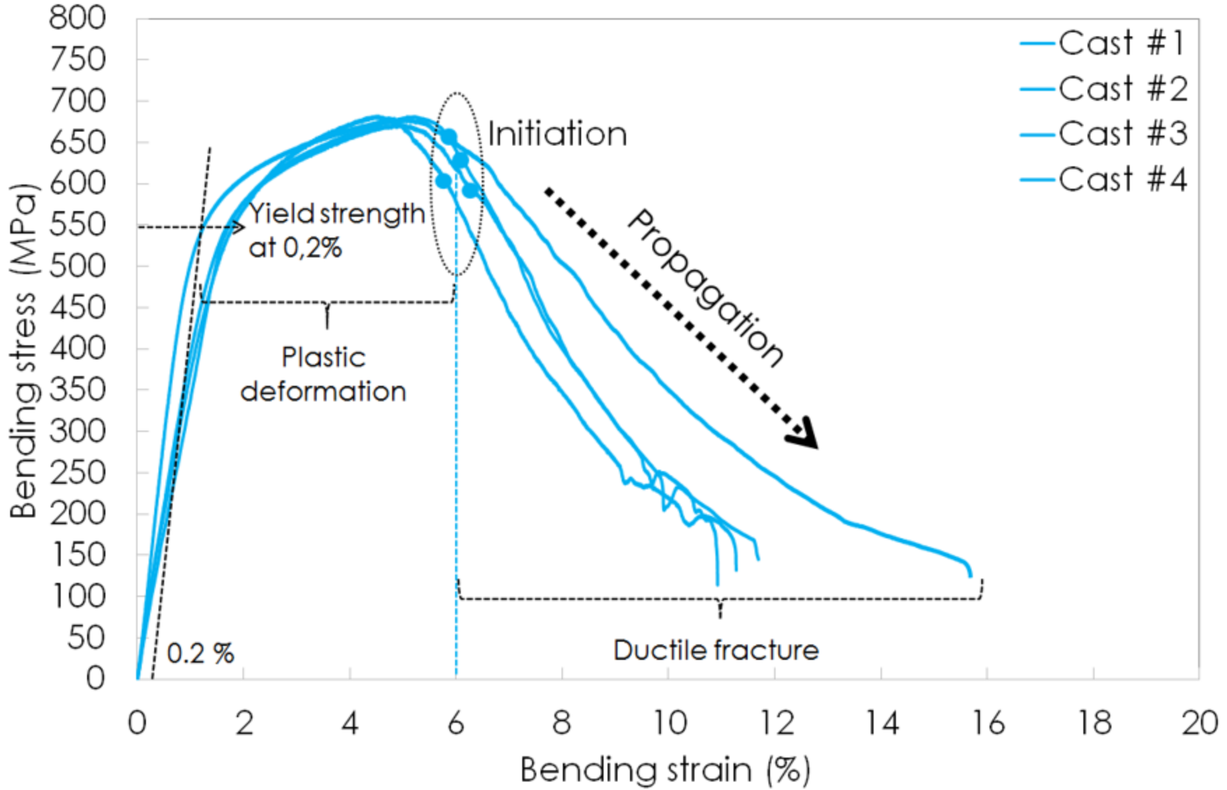
Bending stress (MPa)
Bending strain (%)
Cast #1
Cast #2
Cast #3
Cast #4
Initiation
Yield strength at 0,2%
Plastic deformation
Propagation
0.2 %
Ductile fracture

(b)

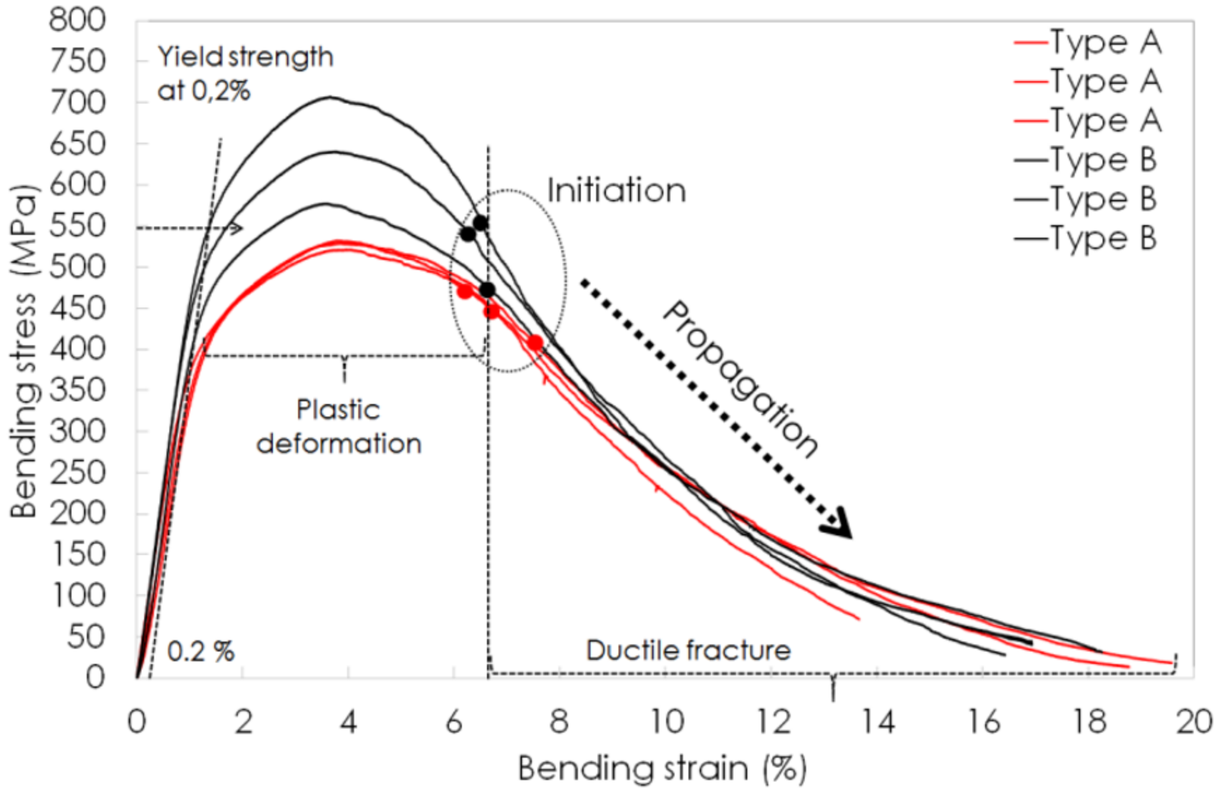
Bending stress (MPa)
Bending strain (%)
Type A
Type A
Type A
Type B
Type B
Type B
Yield strength at 0,2%
Initiation
Plastic deformation
Propagation
0.2 %
Ductile fracture

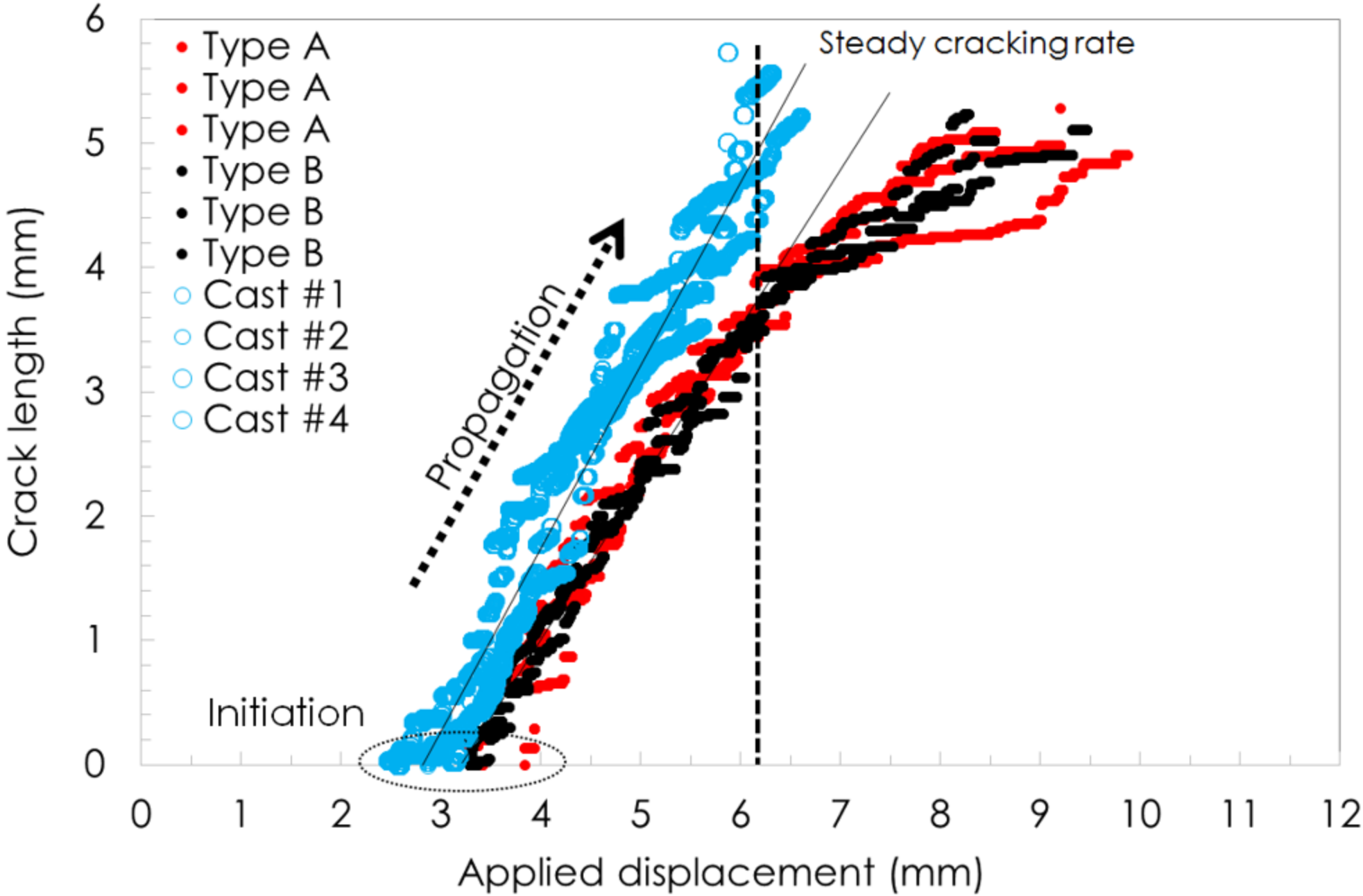
Type A
Type A
Type A
Type B
Type B
Type B
Cast #1
Cast #2
Cast #3
Cast #4
Steady cracking rate
Propagation
Initiation
Crack length (mm)
Applied displacement (mm)
0
1
2
3
4
5
6
7
8
9
10
11
12

(a)

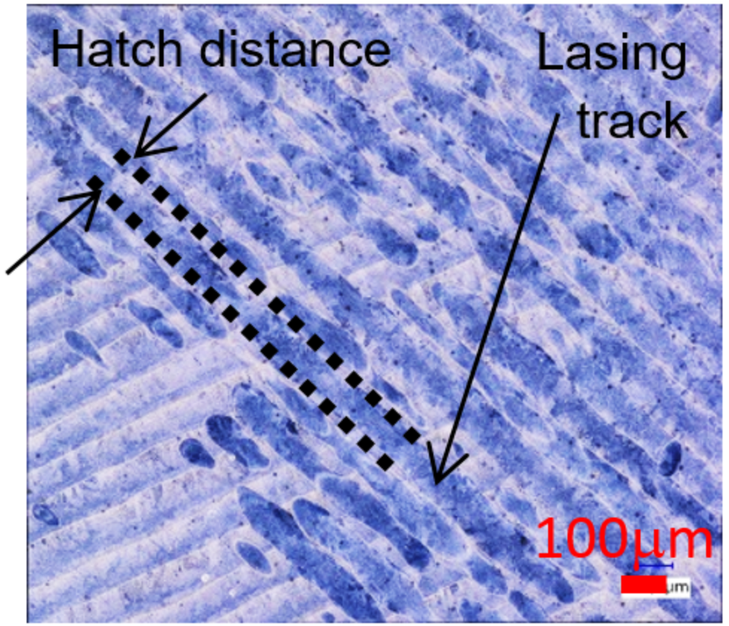

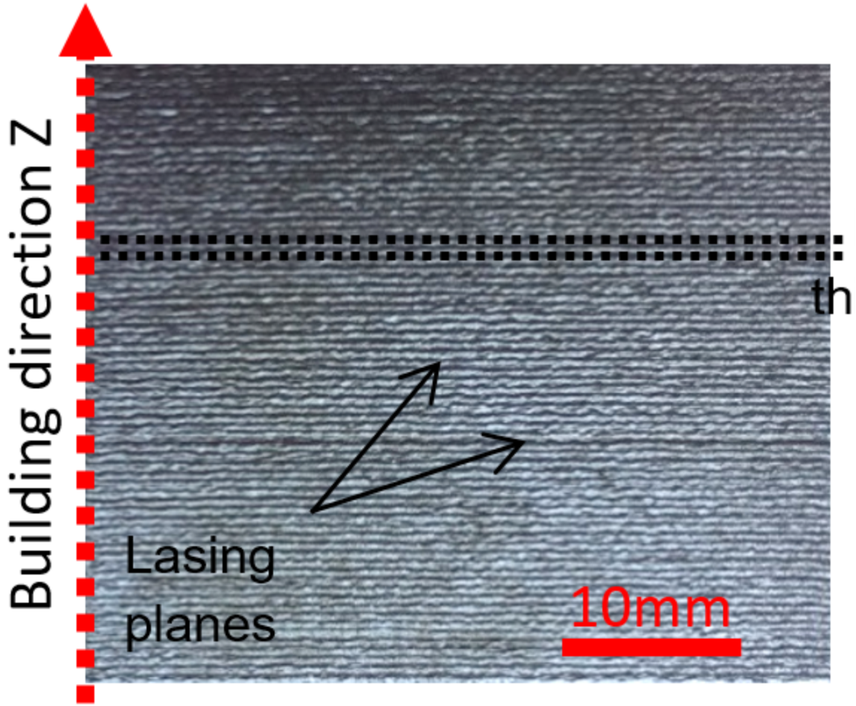

Layer thickness

(b)

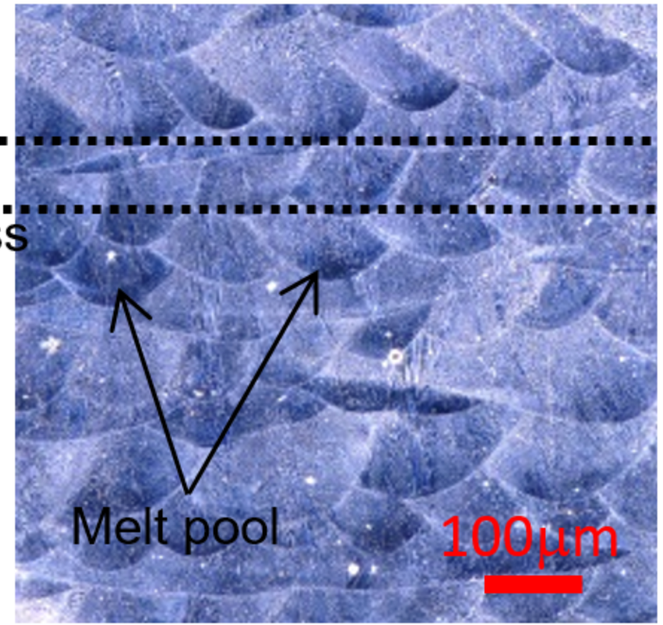

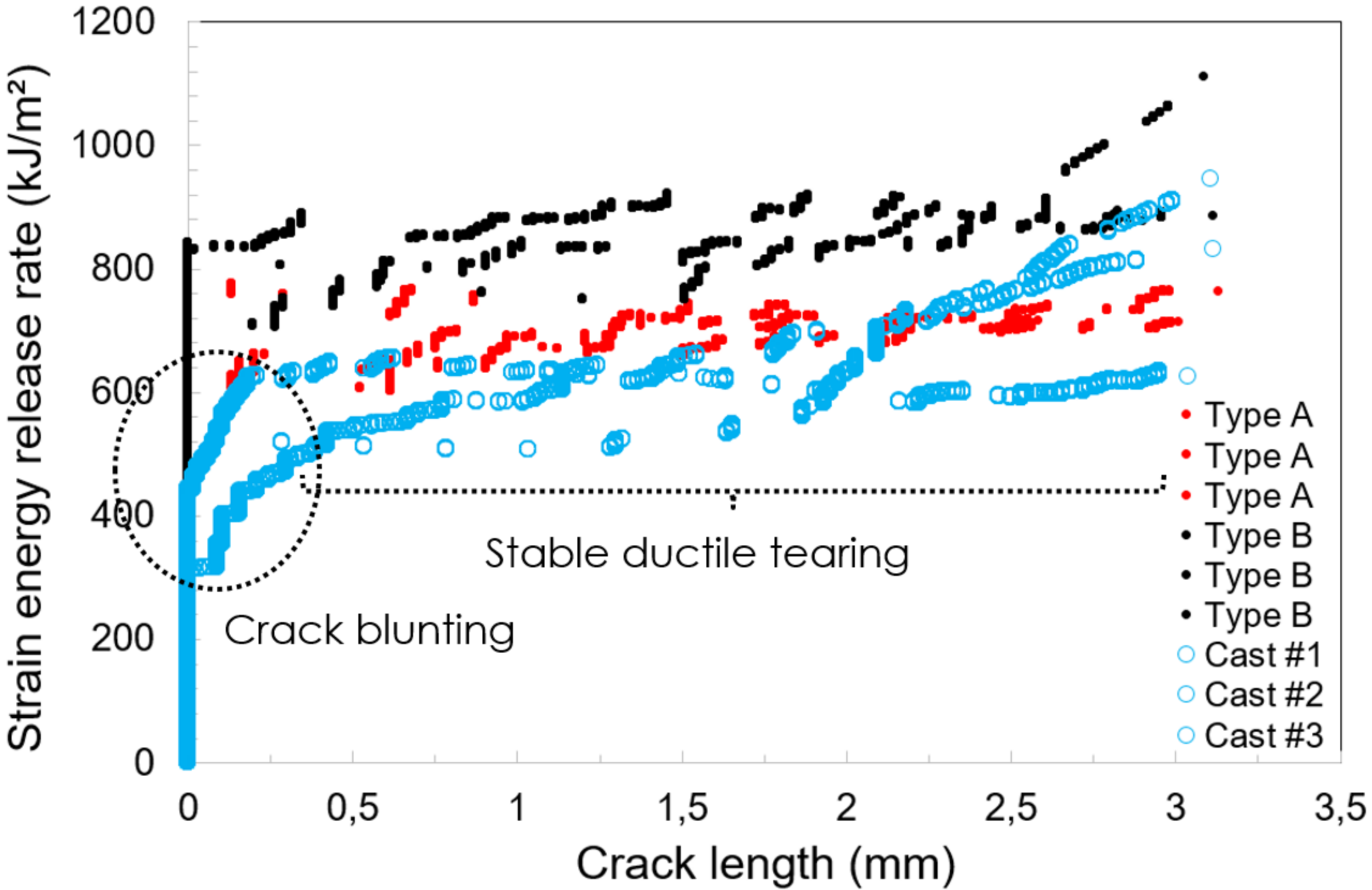
Strain energy release rate (kJ/m²)
1200
1000
800
600
400
200
0
0
0,5
1
1,5
2
2,5
3
3,5
Crack length (mm)
Crack blunting
Stable ductile tearing
Type A
Type A
Type A
Type B
Type B
Type B
Cast #1
Cast #2
Cast #3

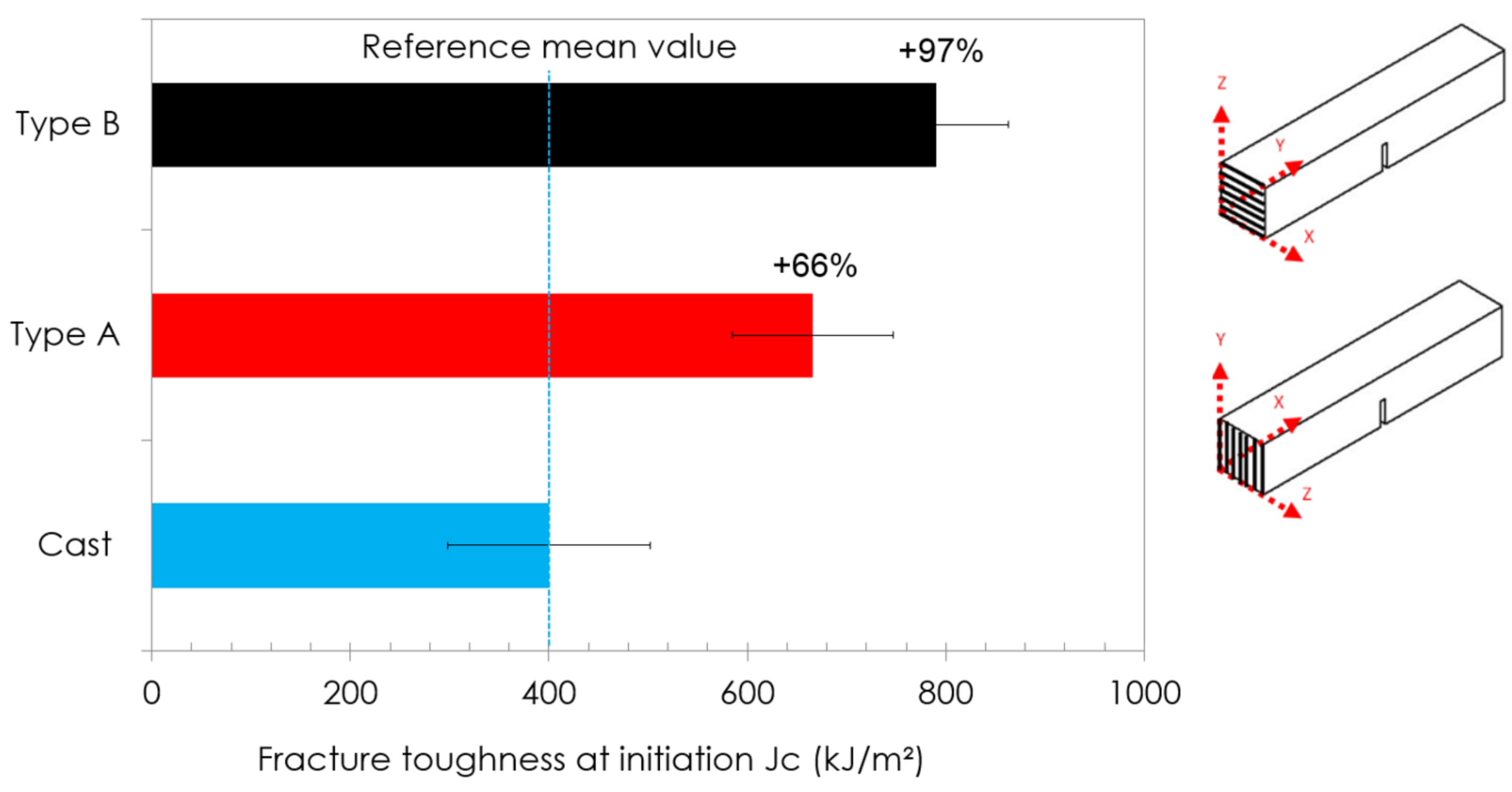
Reference mean value
+97%
+66%
Type B
Type A
Cast
0
200
400
600
800
1000
Fracture toughness at initiation Jc (kJ/m²)
Z
Y
X
Y
X
Z

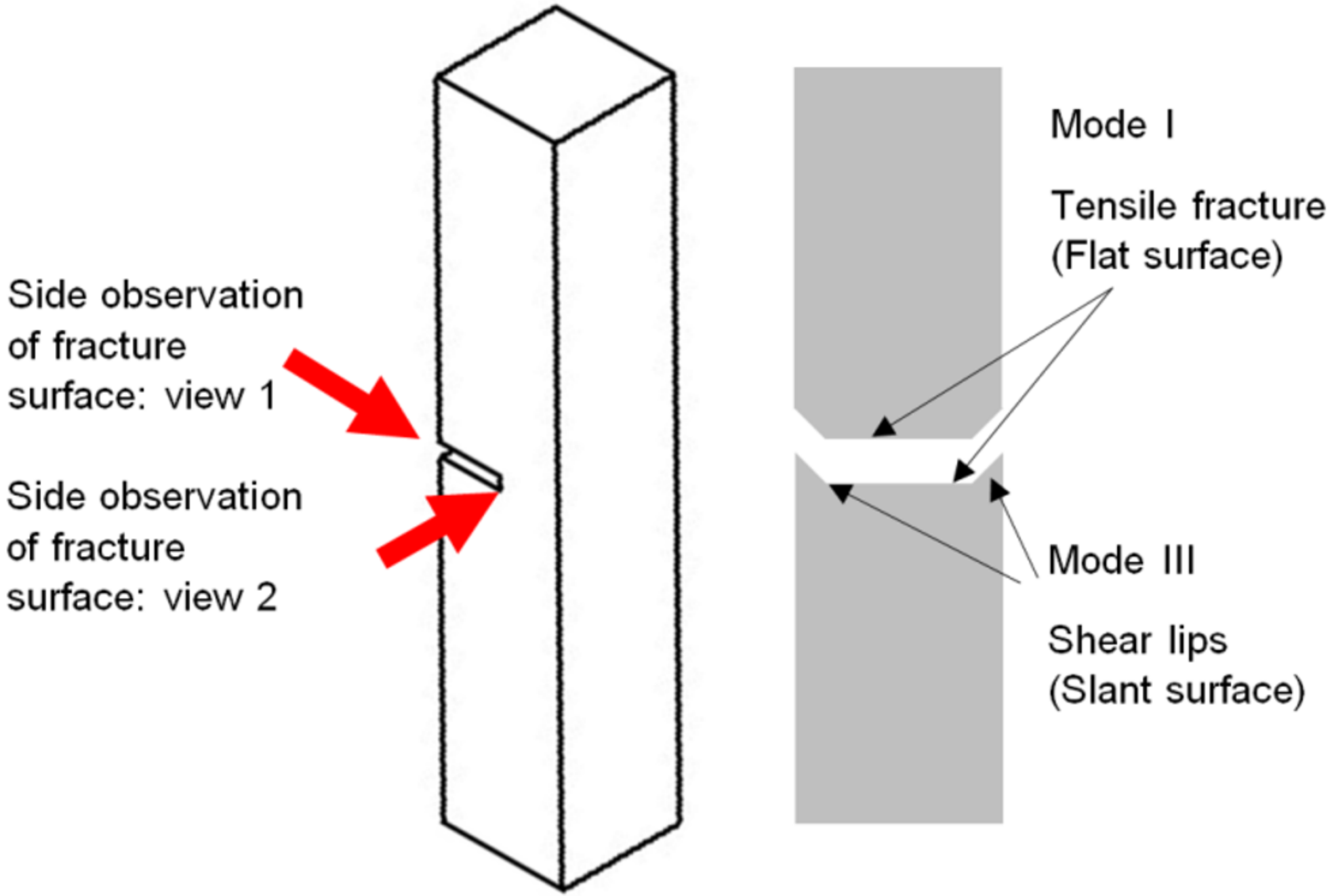
Side observation of fracture surface: view 1
Side observation of fracture surface: view 2
Mode I
Tensile fracture (Flat surface)
Mode III
Shear lips (Slant surface)

(a) Cast

100µm

Crack path

Machined notch

(b) Type A

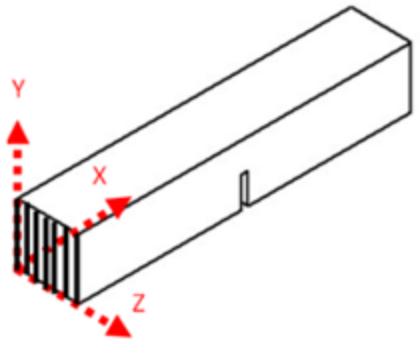

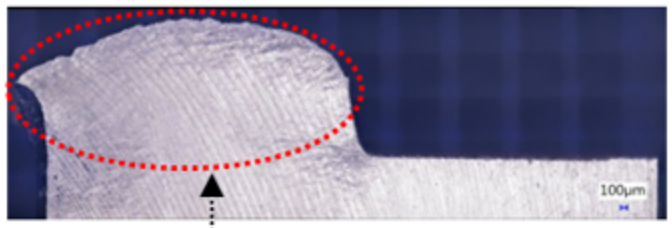

100µm

Extensive plastic deformation

(c) Type B

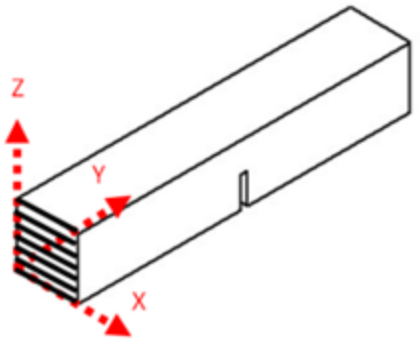

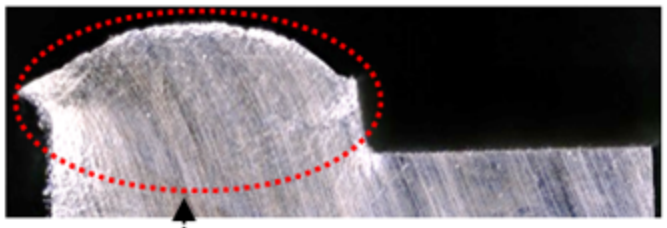

100µm

Extensive plastic deformation

Side views #2

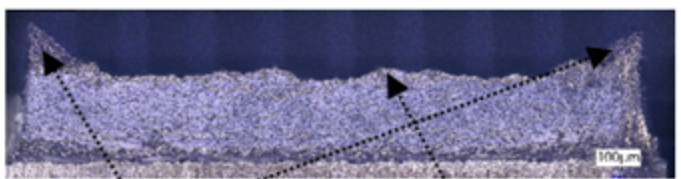

100µm

Minor shear lips: plane stress state

Flat surface : plane strain state

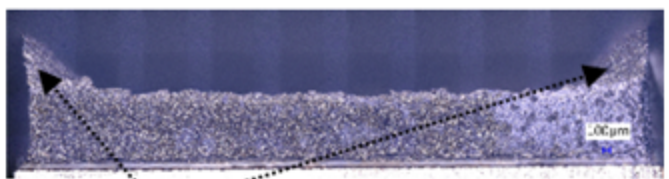

100µm

Minor shear lips

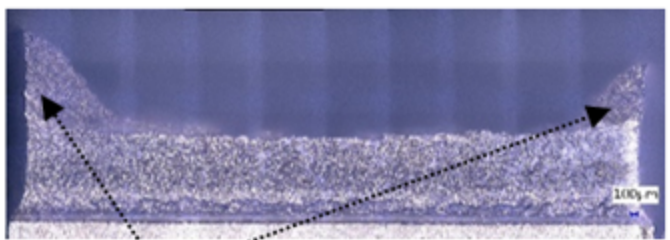

100µm

Major shear lips contributing to the increase in the fracture energy

Side views #1

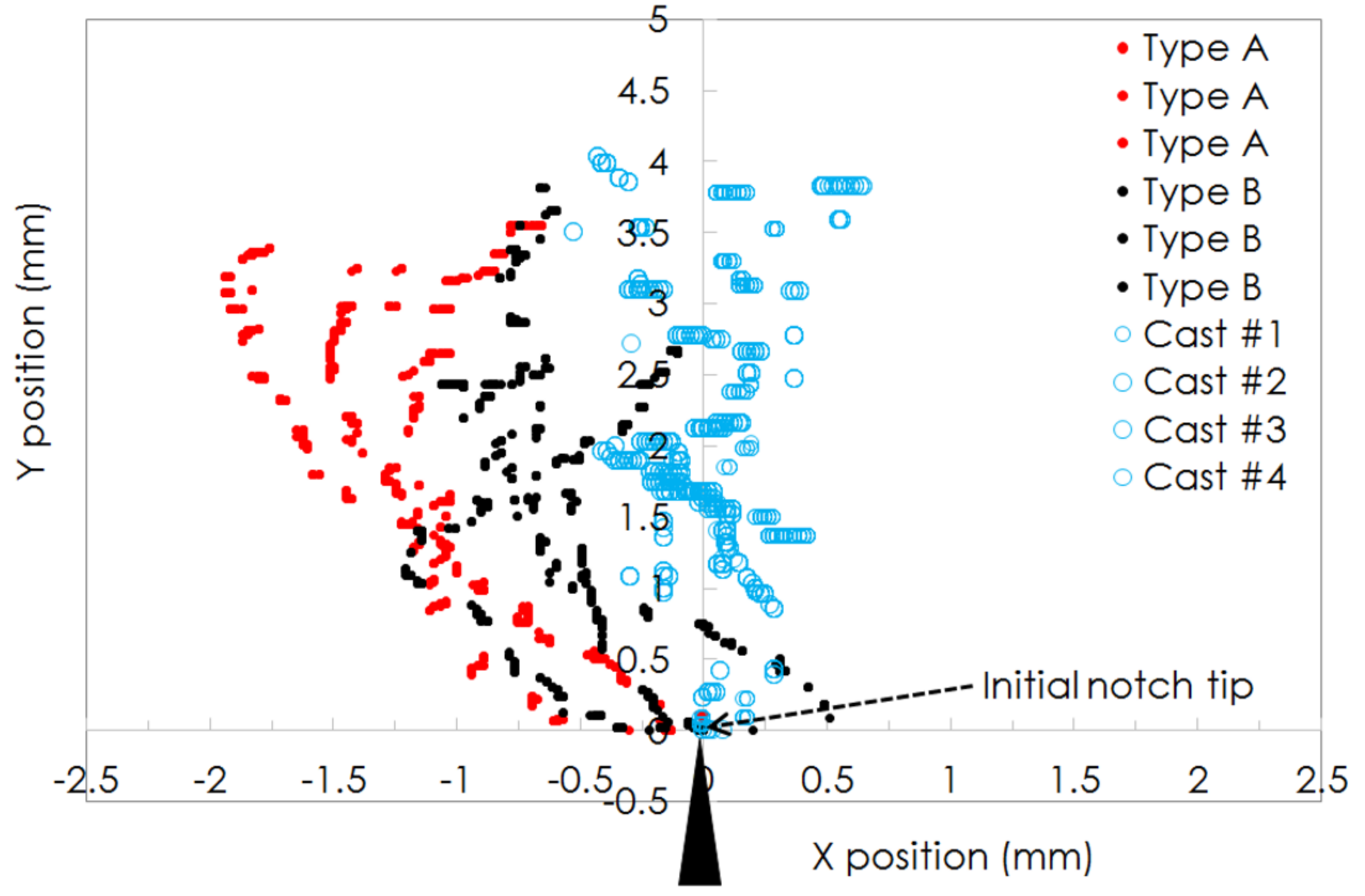
Type A
Type A
Type A
Type B
Type B
Type B
Cast #1
Cast #2
Cast #3
Cast #4
Initial notch tip
Y position (mm)
X position (mm)
5
4.5
4
3.5
3
2.5
2
1.5
1
0.5
0
-0.5
-2.5
-2
-1.5
-1
-0.5
0
0.5
1
1.5
2
2.5

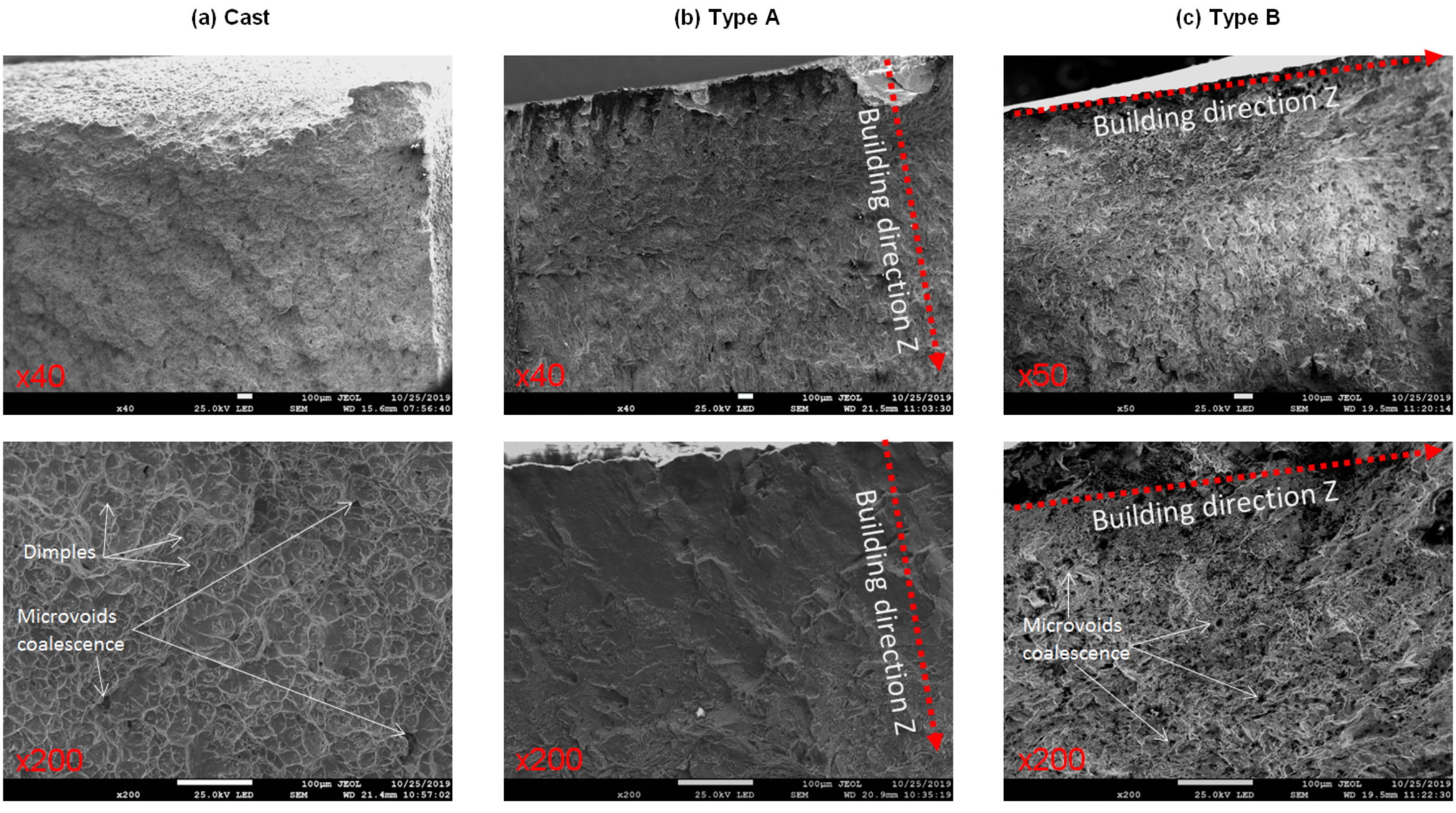
(a) Cast
(b) Type A
(c) Type B
x40
x40
Building direction Z
x50
Building direction Z
Dimples
Microvoids coalescence
x200
x200
Building direction Z
Microvoids coalescence
Building direction Z
x200

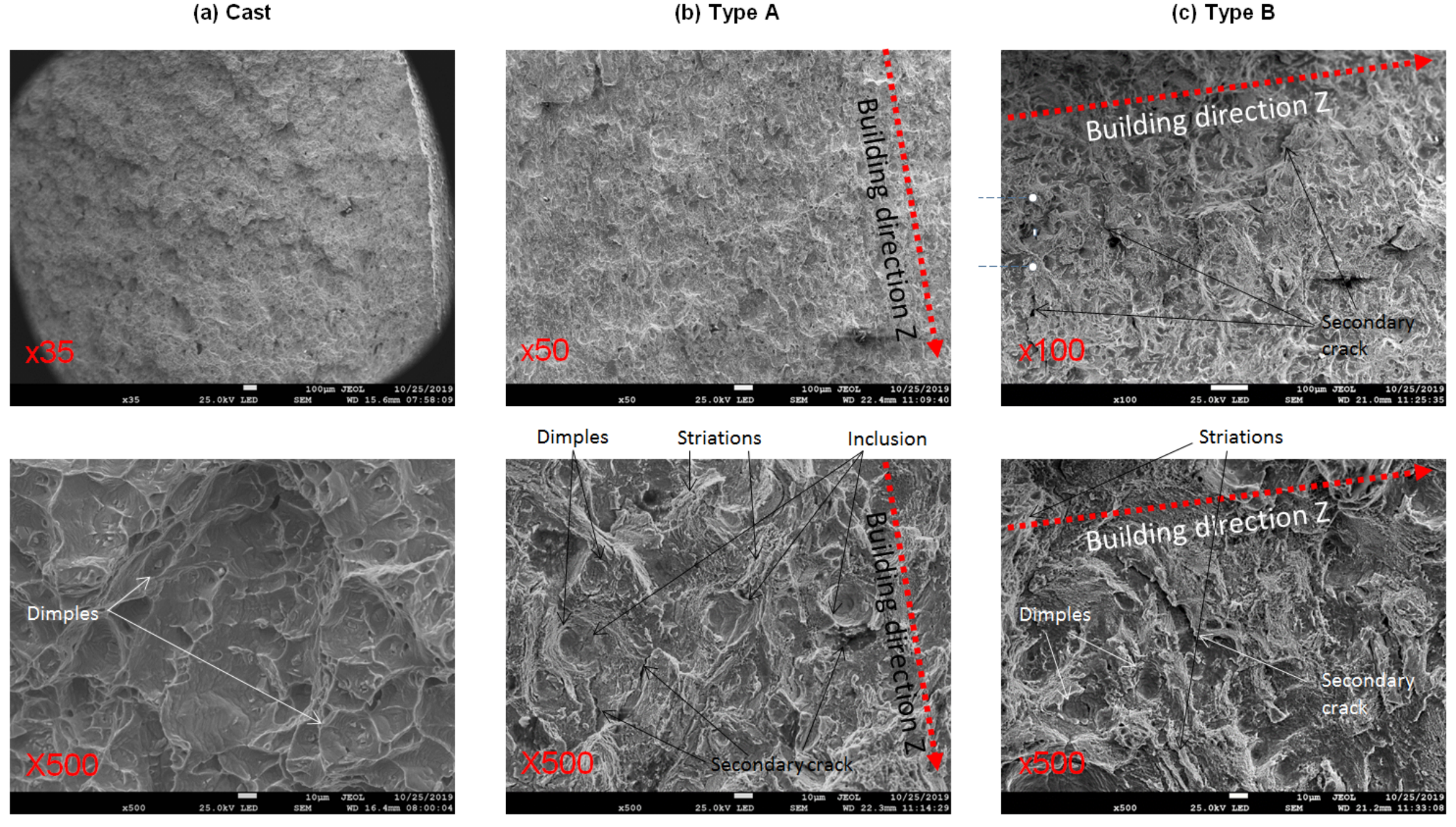
(a) Cast
(b) Type A
(c) Type B
x35
x50
Building direction Z
Building direction Z
x100
Secondary crack
Dimples
X500
Dimples
Striations
Inclusion
X500
Building direction Z
Secondary crack
Striations
Building direction Z
Dimples
Secondary crack
x500

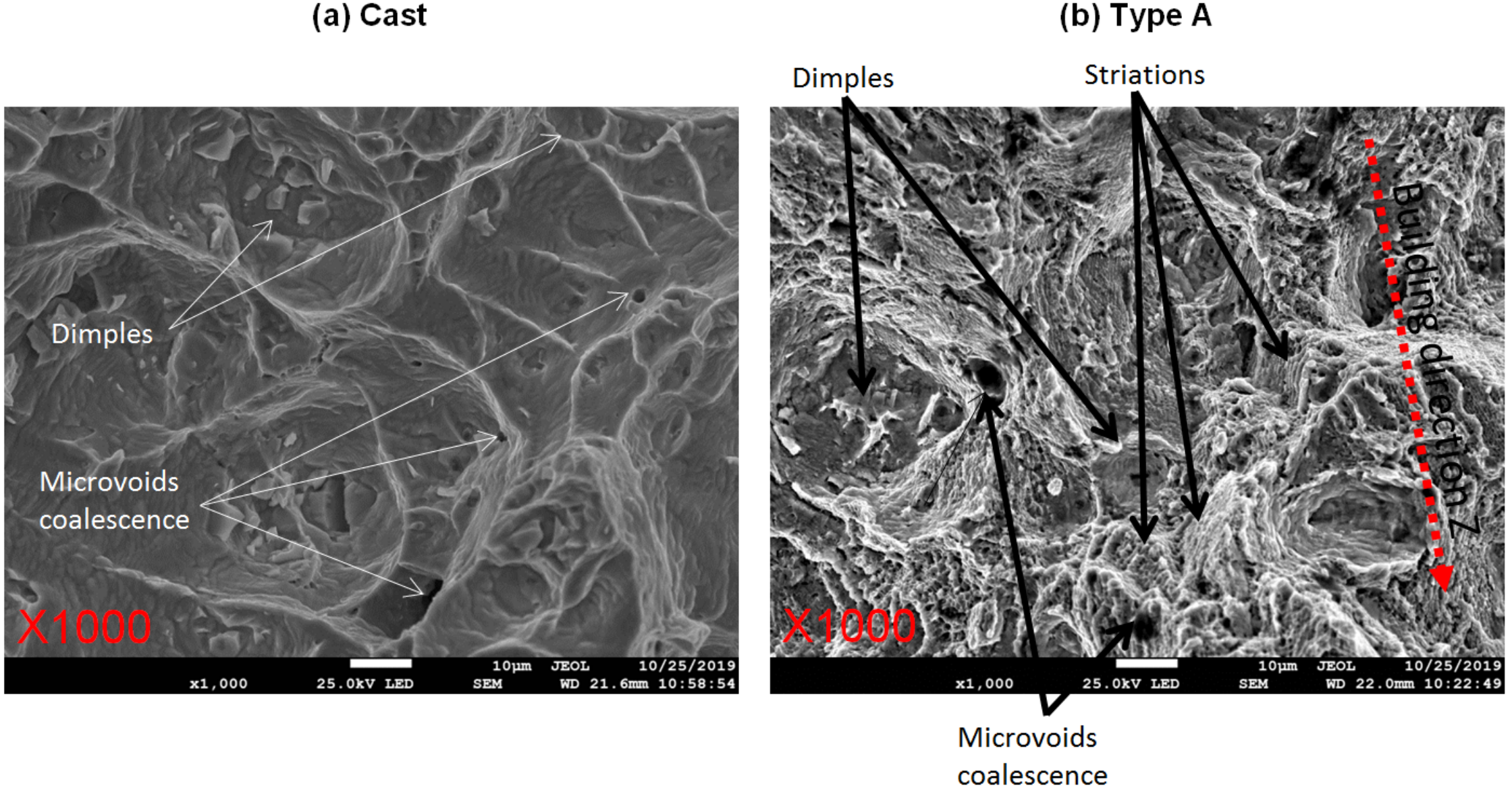
(a) Cast
Dimples
Microvoids
coalescence
X1000
x1,000 25.0kV LED 10µm JEOL SEM WD 21.6mm 10:58:54 10/25/2019
(b) Type A
Dimples
Striations
Building direction Z
X1000
x1,000 25.0kV LED 10µm JEOL SEM WD 22.0mm 10:22:49 10/25/2019
Microvoids
coalescence

Tables

C	Si	Mn	P	S	Cu	Co	Mo	Al	Ti	B	Nb	Ni	Cr	Fe
0.043	0.32	0.18	0.009	0.002	0.07	0.063	2.96	0.68	0.85	0.005	4.93	50.8	17.74	18.74

Tab. 1 – Chemical composition of cast Inconel 718 (source: supplier)

C	Si	Mn	P	S	Cu	Co	Mo	Al	Ti	B	Nb	Ni	Cr	Fe
0.032	0.063	0.031	0.01	0.002	0.024	0.192	2.92	0.501	0.92	0.005	3.28	49.9	18.13	19.11

Tab. 2 – Chemical composition of Inconel 718 powder for AM (source: supplier)

Young modulus (GPa)	Tensile strength (MPa)	Yield strength (MPa)	Elongation at break (%)
192	1330	1085	17

Tab. 3 – Room temperature tensile mechanical properties of cast round bars of Inconel 718

(1010°C hardened tempered - source: supplier)

Laser power (W)	Laser scanning speed (mm/s)	Hatch distance (mm)	Hatch angle (°)
400	1330	0.1	67

Tab. 4 – Manufacturing parameters of AM Inconel 718 specimens

	Grain size (µm)	Aspect ratio	Max PF	GOS (°)
Cast	35±22	0.40	3.3	5.6±2.7
PBF- XY	20±14	0.42	2.3	1.7±0.9
PBF- YZ	21±17	0.30	2.3	1.9±0.8
PBF- XZ	40±20	0.30	3.3	2.0±0.9

Tab. 5 – Results obtained from the SEM-EBSD maps: average grain size, grain shape aspect ratio, the maximum value of pole figure (Max PF) and average Grain Orientation Spread (GOS) for maps shown in Fig. 6.

	Young modulus (GPa)	Ultimate tensile strength (MPa)	Yield strength 0.2% (MPa)	Elongation at break (%)
Cast	174±1	1023±5	855±3	39±2
Type A	153±1	1035±7	740±5	27±1
Type B	211±3	1056±9	800±7	22±1
Type C	236±1	965±10	655±5	27±2

Tab. 6 – Influence of the manufacturing process (cast or PBF AM) on the tensile mechanical properties. Error bars are computed with a confidence index of 95%.

Specimen type	Cast	AM Type A	AM Type B
Yield strength (MPa)	557±5	378±3	499±48
Maximum strength (MPa)	676±6	544±30	626±90

Tab. 7 – Influence of the manufacturing process (cast or PBF AM) on the yield and maximum strengths (with corresponding standard deviation) of Inconel 718 Single Edge Notch specimens subjected to bending loading at ambient temperature